

20 Abstract

21 Precipitation plays an important role in various processes over the Southern Ocean (SO), ranging
22 from the hydrological cycle to cloud and aerosol processes. The main objective of this study is to
23 characterize SO precipitation properties. We use data from the Southern Ocean Clouds Radiation
24 Aerosol Transport Experimental Study (SOCRATES), and leverage observations from airborne
25 radar, lidar, and in situ probes. For the cold-topped clouds (cloud-top-temperature $< 0^{\circ}\text{C}$), the
26 phase of precipitation with reflectivity > 0 dBZ is predominately ice, while reflectivity < -10 dBZ
27 is predominately liquid. Liquid-phase precipitation properties are retrieved where radar and lidar
28 are zenith-pointing. The power-law relationships between reflectivity (Z) and rain rate (R) are
29 developed, and the derived Z - R relationships show vertical dependence and sensitivity to the
30 intermediate drops (diameters between 10-40 μm). Using derived Z - R relationships, reflectivity-
31 velocity (ZV) retrieval method, and a radar-lidar retrieval method, we derive rain rate and other
32 precipitation properties. The retrieved rain rate from all three methods shows good agreement with
33 in-situ aircraft estimates. Rain rate features the prevalence of light precipitation (< 0.1 mm hr^{-1}).
34 We examine the vertical distribution of precipitation properties, and found that rain rate,
35 precipitation number concentration, precipitation liquid water all decreases as one gets closer to
36 the surface, while precipitation size and width increases. We also examine how cloud base rain
37 rate (R_{CB}) depends on cloud depth (H) and aerosol concentration (N_a) for particles with diameter
38 greater than 70nm, and we find a linear relationship between R_{CB} and $H^{3.6} N_a^{-1}$.

39

40 Plain Language Summary

41 Precipitation plays an important role over the Southern Ocean (SO), such as transferring water
42 from air to ocean, and affect cloud and aerosols (tiny airborne particles). The goal of this study is
43 to characterize SO precipitation properties using aircraft data. Aircraft had instruments that can
44 count the number of droplets, as well as lidar and radar, which are remote sensing devices that use
45 laser light and microwave waves respectively to detect objects. Using information from lidar, we
46 can distinguish precipitation phase, and we found that ice precipitation is more frequent when
47 observed radar reflectivity is larger than certain threshold. We derived relationships between rain
48 rate and radar variable that can be used for future research. We also calculated precipitation
49 properties and found our results compares well with direct measurements from the aircraft. Rain
50 rate we calculated features the prevalence of light precipitation. We also studied how precipitation
51 properties very vertically, and found that as one gets closer to the surface, there is a decrease in
52 precipitation number and water, while there is an increase in the size overall. We also found that
53 rain rate depends on how thick the clouds are and on the number of aerosols.

54

55 1 Introduction

56 Surrounding Antarctica, the Southern Ocean (SO) is the second smallest of the five ocean
57 basins, yet it plays an outsized role in the climate system. The SO is estimated to account for about
58 75% of the oceanic heat uptake and about 30-40% of the carbon uptake (Frölicher et al., 2015;
59 Khatiwala et al., 2009), and thus act as a strong buffer against climate change. Due to the lack of
60 anthropogenic aerosols, the SO is also a pristine environment, and it has been argued that SO
61 observations can be used as a present-day proxy for pre-industrial conditions as regards trying to

62 constrain anthropogenic aerosol effects (Hamilton et al., 2014; McCoy et al., 2020), which remain
63 a large source of uncertainty in the climate projections (Lee et al., 2016; Bellouin et al., 2020).
64 More generally, SO clouds, especially low clouds, also have attracted much research interest in
65 recent years because of their importance to the global radiative energy budget (Trenberth and
66 Fasullo, 2010; Bodas-Salcedo et al., 2016; Cesana et al., 2022) as well as global cloud feedbacks
67 and global climate sensitivity (Tan et al., 2016; Zelinka et al., 2020; Mülmenstädt et al., 2021).

68 Precipitation impacts stratocumulus behavior via complex feedbacks that operate on both
69 macrophysical and microphysical scales (Wood, 2012), and has been found to be a key player in
70 the transition of stratocumulus regimes, from closed cells to open cells, and the maintenance of
71 open cells, at least in subtropical stratocumulus (Wang and Feingold, 2009; Yamaguchi and
72 Feingold, 2015; Smalley et al., 2022). Moreover, recent studies highlight the importance of
73 precipitation formation as a dominant sink of cloud condensation nuclei and its control on the
74 cloud droplet number over the SO (McCoy et al., 2020; Kang et al., 2022). Despite the importance
75 of precipitation in low clouds, many climate models and reanalysis data struggle to represent
76 accurately precipitation, including over the SO (Zhou et al., 2021). Mülmenstädt et al., (2021)
77 point out that precipitation biases persist in CMIP6 models, with warm clouds precipitating too
78 frequently, thus shortening the cloud lifetime and underestimating their cooling effect. This
79 problem is especially pernicious for the SO because the error grows in importance, with a reduction
80 in mixed-phase clouds as the climate warms (Bjordal et al., 2020).

81 Due to the remoteness of SO and a general lack of surface and in situ observations, satellite
82 observations have long been an indispensable tool to study SO precipitation. Arguably the best
83 available source of satellite data on SO precipitation rates is CloudSat (W-band radar), which has
84 greater sensitivity to light precipitation than passive sensors (Tansey et al., 2022, Eastman et al.,
85 2019). CloudSat has provided an unprecedentedly broad picture of SO precipitation: Ellis et al.
86 (2009) showed that the precipitation occurrence frequency peaks around 50°-60°S; Mitrescu et al.
87 (2010) found that the SO has a high occurrence of very light precipitation with rain rates smaller
88 than 1 mm h⁻¹ having a frequency of 15%; Mace and Avey (2017) using both CloudSat and
89 Moderate Resolution Imaging Spectroradiometer (MODIS) data found that precipitation processes
90 in SO warm clouds vary seasonally with a stronger precipitation susceptibility to cloud droplet
91 number in winter. Although compared to other satellite measurements, CloudSat better detects
92 light precipitation and is better able to determine the rain rate, CloudSat is nonetheless affected by
93 ground clutter which severely corrupts the reflectivity measurements within about 750 m of the
94 surface (Marchand et al., 2008). CloudSat precipitation retrievals are also largely limited to
95 situations where the measured near-surface (750 to 1000m) reflectivity is larger than -15 dBZ
96 (Haynes et al., 2009), although the precipitation is often observed falling for SO clouds with
97 reflectivity factors less than -15 dBZ (e.g., Mace and Protat 2018). As shown by Tansey et al.
98 (2022), who evaluated CloudSat retrievals using surface precipitation measurements during the
99 Macquarie Island Cloud Radiation Experiment (MICRE), the CloudSat 2C-Precip-Column
100 product misses most precipitation with a precipitation rate less than 0.5 mm hr⁻¹. In addition,
101 CloudSat radar reflectivity measurements provide very limited information regarding the phase of
102 the precipitation. The current operational CloudSat precipitation products categorize precipitation
103 into liquid, snow, or mixed phase based largely on temperature profiles extracted from ECMWF
104 analysis and identifying melting layers, rather than any directly measured quantity.

105 In the face of biases and uncertainty in satellite retrievals and modeling, precipitation
106 observations from multiple sources such as islands, ships, and aircraft provide us with an important

107 opportunity to obtain a more detailed view of SO precipitation. Such precipitation observations
108 were made in several recent collaborative field campaigns (McFarquhar et al., 2021), including the
109 aforementioned Macquarie Island Cloud Radiation Experiment (MICRE) during 2016-2018, the
110 Clouds Aerosols Precipitation Radiation and atmospheric Composition over the Southern Ocean
111 (CAPRICORN) campaign in 2016 and 2018, the Measurements of Aerosol, Radiation, and Clouds
112 over the Southern Ocean (MARCUS) campaign during 2017-2018, and the Southern Ocean Cloud
113 Radiation and Aerosol Transport Experimental Study (SOCRATES) during Jan-Feb 2018. For
114 example, Tansey et al. (2022) created a 1-year “blended” surface precipitation dataset (which
115 combines W-band radar, tipping bucket and disdrometer data) for MICRE and used these data to
116 study the diurnal, synoptic and seasonal variability of near-surface precipitation. These authors
117 found that total accumulation was comprised of about 74% rain, 16% ice or mixed phase
118 precipitation, and 10% small particle precipitation. In a study based on the CAPRICORN datasets.
119 Montoya Duque et al. (2022), applied a K-means clustering technique to radiosonde data to
120 classify the atmosphere into seven thermodynamic clusters, and found that the highest occurrence
121 of surface precipitation was associated with warm frontal clusters and high-latitude cyclone
122 clusters (poleward of the polar front near cyclones), with warm rain dominating in the former and
123 the largest fraction of snow in the latter. Shipborne precipitation observations from CAPRICORN
124 have also been included along with observations from other research vessels in the Ocean Rain
125 and Ice-Phase Precipitation Measurement Network (OceanRAIN), the first global and
126 comprehensive along-track in-situ water cycle surface reference dataset (Klepp et al., 2018). Protat
127 et al. (2019a,b) used OceanRAIN data to investigate discrepancies among satellite products at high
128 latitudes and found large latitudinal and convective-stratiform variability in the drop size
129 distribution (DSD). Protat et al. (2019a) pointed out that the Southern hemisphere high latitudes
130 stood out as regions with a systematically higher frequency of occurrence of light precipitation
131 with rates $< 1 \text{ mm h}^{-1}$ and difference in the shape parameter μ in the precipitation drop size
132 distribution (DSD), with high-latitude and midlatitude μ ranging from -1 to 1, which is lower than
133 the assumed μ of 2 or 3 in the Global Precipitation Measurement Mission (GPM) rainfall
134 algorithms (Greco et al., 2016; Seto et al., 2013). Protat et al. (2019b) found that the Southern
135 Hemisphere high latitude (-67.5°S to -45°S), along with Northern Hemisphere polar latitude
136 bands, stood out with a fundamentally different relationship between radar observables and rainfall
137 properties, such as radar reflectivity to rain rate (Z-R) relationship, mainly because of much lower
138 rain rates over the SO, suggesting that specific relationships are needed for these regions.

139 In this study, we use data collected during SOCRATES to study the precipitation properties
140 of summertime SO stratocumulus, leveraging observations from airborne W-band HIAPER Cloud
141 Radar (HCR), High Spectral Resolution Lidar (HSRL), and in situ probes. In particular we
142 examine occurrence of liquid and ice phase precipitation, and for liquid precipitation we derived
143 precipitation properties such as rain rate, using a hierarchy of retrieval methods from simple Z-R
144 relationships to more complex radar reflectivity-velocity retrieval (ZV retrieval) and radar-lidar
145 retrievals. We also apply the precipitation observations and retrievals to study the in-and-below
146 cloud precipitation properties and rain rate dependence on cloud depth and aerosol concentration.

147 This paper is organized as follows: Section 2 introduces the datasets, instruments, as well
148 as the analysis and retrieval methods used in this study. Section 3 provides a campaign overview
149 and discusses phase partitioning. Section 4 examines Z-R relationships and precipitation retrievals
150 and compares these remote sensing data to in situ measurements. Section 5 provides a statistical

151 summary of the precipitation properties, and Section 6 explores the relationship of stratocumulus
 152 rain rate with cloud depth and aerosol concentration, ending with conclusions in Section 7.

153

154 **2 Data and Methods**

155 In this section we introduce the data and methods that we use to characterize in-and-below cloud
 156 precipitation properties. Section 2.1 describes the SOCRATES campaign sampling strategies,
 157 remote sensors (W-band Cloud Radar, HCR, and High Spectral Resolution Lidar, HSRL), and in
 158 situ instruments. Section 2.2 describes how we use in situ data to analyze in-cloud and below-
 159 cloud precipitation properties, as well as how we estimate Z-R relationships. In section 2.3, we
 160 describe reflectivity-velocity (ZV) and radar-lidar retrievals.

161 2.1 Instrumentation and data

162 In this study, we use data collected during the SOCRATES campaign to study the precipitation
 163 properties of stratocumulus. The SOCRATES campaign happened in January-February 2018
 164 (McFarquhar et al., 2021), when the NSF/NCAR Gulfstream GV aircraft conducted 15 research
 165 flights over the SO. After taking off from Hobart (Tasmania), the aircraft typically flew south at
 166 high altitude and then descended to just above cloud top for several 10's of minutes, before heading
 167 back towards Hobart. On the return, the aircraft would descend into low cloud and sample aerosols,
 168 clouds, and precipitation with a repeating series of activities that included in-, below-, and above-
 169 cloud level legs (where the aircraft flew at a nearly fixed altitude), as well as sawtooth legs (where
 170 the aircraft ascended or descended through the cloud layer). Supplementary Figure S1 shows a
 171 schematic of the typical flight, as well as the 15 flight tracks flown during SOCRATES.

172 To characterize in-and-below cloud precipitation properties, we leverage observations from both
 173 in situ probes and remote sensors. Table 1 gives a summary of the instruments we use in this study,
 174 along with a primary reference for each instrument. We describe how these in situ probe data are
 175 used in Section 2.2.

176

177 **Table 1.** Instruments

178

| Instruments | Measurements | References |
|------------------------------------|--|---|
| Cloud Droplet Probe (CDP) | Size and concentration of hydrometeors with a diameter between 2-50 μm | Lance et al. (2010) https://data.eol.ucar.edu/dataset/552.002 |
| Two-Dimensional Stereo probe (2DS) | Size and concentration of hydrometeors with a diameter between 10-1280 μm | Wu and McFarquhar (2019) https://data.eol.ucar.edu/dataset/552.047 |
| Ultra-High-Sensitivity Aerosol | Aerosols with dry diameters between 60 and 1,000 nm | DMT(2013); Sanchez et al. (2021) https://data.eol.ucar.edu/dataset/552.002 |

Spectrometer
(UHSAS)

| | | |
|---------------------------------------|---|---|
| HIAPER Cloud Radar (HCR) | Reflectivity, Doppler velocity, Spectral width, Signal to noise ratio, etc. | Vivekanandan et al. (2015) https://data.eol.ucar.edu/dataset/552.034 |
| High Spectral Resolution Lidar (HSRL) | Backscatter coefficient, Particle Linear Depolarization Ratio, Extinction coefficient, etc. | Eloranta (2005) https://data.eol.ucar.edu/dataset/552.034 |

179

180 *Note: For both CDP and 2DS, data is available at 1Hz temporal resolution. CDP data can be found in*
 181 *SOCRATES Navigation, State Parameter, and Microphysics Flight-Level Data. This study uses version 1.4*
 182 *of this dataset. This study uses version 1.1 of the 2DS dataset. The radar and lidar moments data version*
 183 *3.1 were processed by NCAR/EOL and 2 Hz (0.5 seconds) temporal resolution and 19 meters range vertical*
 184 *resolution. The operational specifications of HCR and HSRL is available at*
 185 https://data.eol.ucar.edu/datafile/nph-get/552.034/readme_HCR_HSRL_SOCRATES_2Hz_v3.1.pdf.

186

187 Remote sensors include a 94-GHz W-band HIAPER Cloud Radar(HCR) (Vivekanandan et al.,
 188 2015) and a 532-nm High Spectral Resolution Lidar (HSRL) (Eloranta, 2005). Based on radar and
 189 lidar moments data, we will use retrieval techniques to derive precipitation properties, as detailed
 190 in section 2.3. HCR and HSRL were deployed in previous campaigns, such as CSET (e.g. Schwartz
 191 et al., 2019). The radar and lidar data were processed by NCAR/EOL at 2 Hz (0.5 seconds)
 192 temporal resolution and have 19 m vertical range resolution. A description of the NCAR/EOL
 193 data processing and corrections are given in readme files that are distributed with the data (with
 194 link in the acknowledgement). This includes a correction of radial velocity for platform motion
 195 following Romatschke et al. (2021), in which corrections are applied to the nadir and zenith
 196 pointing data separately. For nadir pointing data, radial velocity was corrected following Ellis et
 197 al. (2019), where for radial velocity of the surface (assumed to be 0 m/s) is used as a reference to
 198 correct the data with a running 3rd degree polynomial filter. A similar method is applied to the
 199 zenith pointing data, which are the focus of this paper. But for the zenith pointing data, instead of
 200 assuming zero velocity of surface, it is assumed that the cloud top velocities from zenith pointing
 201 times are similar to those of the neighboring nadir pointing times. Specifically, cloud top velocities
 202 are first calculated for both the nadir pointing data and zenith pointing data, then the difference of
 203 the two is used to correct the bias in the zenith pointing velocity data. Figure S2 shows an example
 204 of the zenith pointing velocity fields before and after the correction, and Figure S3 shows the
 205 averaged nadir pointing and zenith pointing velocity profiles from RF13, demonstrating that
 206 correction resulted in consistent velocity profile between nadir pointing data and zenith pointing
 207 times.
 208

209 2.2 In situ Measurements

210 2.2.1 Droplet size distribution

211 This study uses in situ measurements mainly from two particle-sizing-instruments: a Cloud
 212 Droplet Probe (CDP) and a Two-Dimensional Stereo probe (2DS) as listed in Table 1. We focus
 213 on in situ measurement from these legs (as marked in Figure S1): below-cloud level legs, in-cloud
 214 level legs, and sawtooth legs (which are further divided into top-half of the cloud, bottom-half of
 215 the cloud, and the below-cloud portion as described below). These in situ measurements will be
 216 used to derive reflectivity to rain rate relationships (Z-R) relationships (section 4.1), to validate the
 217 precipitation retrievals (section 4.3), and to study in-and-below cloud precipitation properties
 218 (section 5).

219 We combine measurements from CDP and 2DS to create combined droplet size distribution (DSD)
 220 by using CDP measurements for bins with a diameter $< 25\mu\text{m}$ and 2DS for bins $> 50\mu\text{m}$. For
 221 drops in the intermediate size range (25–50 μm) we take the larger values of the two probes. After
 222 combining the DSD from two probes, we further averaged DSD for different regions and flight
 223 segments. Specifically, we examine the top half of the cloud layer from sawtooth legs; the bottom
 224 half of the cloud layer from sawtooth legs; the below-cloud portion of the sawtooth legs; the below-
 225 cloud level legs in 20s intervals; and in-cloud level legs in 10s intervals. For the purpose of
 226 averaging the in-situ data into these categories, we define the aircraft as in-cloud when then liquid
 227 water content greater than 0.03 g m^{-3} (Wood et al., 2011; Kang et al., 2021). Because of the limited
 228 sampling volumes of the probes, even with averaging, there can be gaps (and large variability) in
 229 the DSD distribution for large particles (where the concentrations are sufficient low that the probes
 230 become increasingly unlikely to observe these particles). As needed, we fill gaps in the DSD by
 231 fitting an exponential curve following Comstock et al. (2004) and extrapolate DSD for larger
 232 particles (out to a diameter of 2000 μm).

233

234 2.2.2 Precipitation properties

235 Precipitation properties are derived using the DSD. For different segments, we calculated rain rate
 236 (liquid water flux) as:

237

$$R = 3600 * \frac{\pi}{6} \rho_w \int_{D_{min}}^{\infty} n(D) D^3 v_f(D) dD \quad (1)$$

238 where ρ_w is the density of liquid water (1000 kg m^{-3}), D is the diameter in of m, 3600 is a scaling
 239 factor to convert the unit from $\text{kg m}^{-2} \text{s}^{-1}$ to mm hr^{-1} , and $v_f(D)$ is the terminal fall velocity (unit
 240 of m s^{-1}) of droplets in the range from D to $D+dD$, and $n(D)$ is the drop size distribution (with
 241 units of $\text{m}^{-3} \text{mm}^{-1}$). We use the terminal fall velocity model of Beard (1976) for $v_f(D)$ term. D_{min}
 242 is the lower limit for the integration, and except where stated otherwise is set to $40\mu\text{m}$. In Section
 243 4.1, we test the importance of smaller droplets with diameter smaller than $40\mu\text{m}$ on the liquid
 244 water flux($\text{LWF}_{\text{total}}$).

245 Similarly, precipitation number (N_{precip}) is calculated as:

246

$$N_{precip} = \int_{D_{min}}^{\infty} n(D) dD \quad (2)$$

247 Precipitation liquid water content (LWC_{precip}) is calculated as:

248

$$LWC_{precip} = \frac{\pi}{6} \rho_w \int_{D_{min}}^{\infty} n(D) D^3 dD \quad (3)$$

249 Precipitation liquid water content weighted mean diameter (D_{precip}), which can be thought of as
250 diameter at which half of LWC_{precip} is below and half is above, is calculated as:

251

$$D_{precip} = \frac{\int_{D_{min}}^{\infty} n(D) D^4 dD}{\int_{D_{min}}^{\infty} n(D) D^3 dD} \quad (4)$$

252 Precipitation liquid water content weighted width (σ_{precip}) is calculated as:

253

$$\sigma_{precip} = \sqrt{\frac{\int_{D_{min}}^{\infty} n(D) D^3 (D - D_{precip})^2 dD}{\int_{D_{min}}^{\infty} n(D) D^3 dD}} \quad (5)$$

254

255 2.2.3 Z-R relationships

256

257 To estimate the Z-R relationships from in situ measurements, we calculated radar reflectivity Z
258 and rain rate R, respectively from the in situ droplet size distributions (DSD). Rain rate is
259 calculated as equation 1. Reflectivity is proportional to the sixth moment of the DSD:

$$Z = \int_0^{\infty} n(D) D^6 \gamma_f(D) dD \quad (6)$$

260 where $n(D) dD$ gives number concentrations from diameter D to $D+dD$, $\gamma_f(D)$ is the Mie-to-
261 Rayleigh backscatter ratio (shown in Figure S4, which is the ratio of the backscatter efficiency of
262 Mie scattering for W-band (94-GHz), calculated using the miepython package based on Wiscombe

263 (1979), and backscatter efficiency of Rayleigh scattering (Bohren & Huffman, 1983). With
 264 calculated reflectivity and rain rate from the in situ DSD, the Z-R relationship assumes a traditional
 265 power-law of the form:

$$Z = aR^b \quad (7)$$

266 Where a and b are coefficients, and Z is the independent variable. Equation 7 can also be
 267 rearranged as $R = (Z/a)^{1/b}$, which can be used to derive R based on Z observations. Coefficients
 268 a and b can be estimated using the least-squares regression in log space following Comstock et al.
 269 (2004):

$$\log R = \frac{1}{b} (-\log a + \log Z) \quad (8)$$

270 We estimated the uncertainty in estimated exponents b and intercepts a that are based on in situ
 271 data using bootstrapping. Note that in section 4.1, we also estimated Z-R relationship based on
 272 radar observed reflectivity factor and rain rate from radar-lidar retrieval (more details in section
 273 2.3.3), where we use moving blocks bootstrapping method following Wilks (1997) to estimate
 274 uncertainty in a and b coefficients, with a block length that close to the unfolding length.

275 2.3 Precipitation Retrievals based on remote sensors

276 Precipitation retrievals described in this section use the zenith-pointing data collected when the
 277 aircraft was flying level-legs below the cloud. To illustrate, Figure 1a shows the flight track altitude
 278 and measured radar reflectivity for research flight 13 (RF13). In panel (a), the portions of the flight
 279 track which feature below-cloud-level legs are colored green. Figure 1b-f shows the radar and lidar
 280 data in more detail, for the below-cloud level leg starting from 03:40 UTC, which is marked by
 281 the grey shading in Figure 1a. In general, retrievals undertaken for below-cloud level legs have the
 282 advantage that the zenith pointing lidar data allows one to determine the position of cloud base, as
 283 well as providing measurements of the backscatter (Figure 1c) and depolarization ratio (Figure 1d)
 284 of the precipitation that has fallen from the cloud and can be used to determine the precipitation
 285 phase. We describe the retrieval process in the three subsections that follow: (1) determine the
 286 cloud boundaries; (2) determine the phase of precipitation; (3) determine the liquid precipitation
 287 microphysical properties (such as the rain rate).

288 2.3.1 Determine the cloud boundaries

289 To determine the cloud base, we use the lidar backscatter coefficient β (e.g. Figure 1c) and define
 290 the cloud base as the altitude where β first exceeds a threshold of $0.0001 \text{ m}^{-1} \text{ sr}^{-1}$. The black dots
 291 in Figure 1c show the cloud base identified using this threshold. Cloud top for our analysis is
 292 based on the radar reflectivity data, which has already been masked for significant detections
 293 (above the instrument noise floor). The cloud top is taken simply as the maximum height with a
 294 valid reflectivity echo below 3km, as marked by grey dots in Figure 1b-f.

295 2.3.2 Determine the phase of precipitation below cloud base

296 With the cloud boundaries identified, the next step is to determine the phase of the precipitation
 297 falling from the clouds. Following Mace and Protat (2018), we determine the precipitation phase

298 using the lidar particle linear depolarization ratio (PLDR) (e.g., Figure 1d). The basic concept is
 299 that the lidar emits linearly polarized light, and scattering by spherical particles (e.g. liquid drops)
 300 does not change the polarization state of the light and thus generates little PLDR, while scattering
 301 from non-spherical particles (e.g. ice particles) creates significant depolarization and thus
 302 generates measurable increase in PLDR. In this study, for each lidar column, we examined the
 303 median of the PLDR over the vertical interval between cloud base to the first useable lidar range
 304 gate. For clouds with a cloud top temperature greater than 0, that is for warm clouds whose
 305 precipitation must be liquid, we find the below-cloud base PLDR values to be less than 0.03 about
 306 90% of the time, and to be above 0.05 less than 1% of the time(see Figure S5 for overall statistics
 307 and Figure S6 for an example case). Thus, for cooler cold-topped clouds (which might precipitate
 308 ice), we define the precipitation to be liquid phase when the median PLDR < 0.03; ice precipitation
 309 when PLDR > 0.05; and ambiguous phase with PLDR values in between.

310 2.3.3 Liquid Precipitation retrieval

311 After determining the cloud base and precipitation phase, we can use a hierarchy of retrieval
 312 methods with increasing complexity to derive the precipitation microphysical properties, starting
 313 from (1) a simple Z-R relationship approach where only one variable, the radar reflectivity, Z, is
 314 available to derive the rain rate, to (2) a ZV retrieval following Mace et al. (2002) and Marchand
 315 et al. (2007), where radar reflectivity, Z, and mean Doppler velocity, V, are known to (3) a radar-
 316 lidar retrieval following O'Connor et al. (2005) based on three observables: radar reflectivity Z,
 317 radar Doppler spectral width σ_d , and lidar backscatter β . We briefly describe the radar-lidar and
 318 then the ZV and in this section, and present retrieval results and evaluate the retrievals using in
 319 situ observations in Section 4.

320 The radar-lidar retrieval technique uses three input variables radar reflectivity, Z (Figure 1b),
 321 doppler spectral width, σ_d (Figure 1e), and lidar backscatter, β (Figure 1c), to solve for three
 322 parameters in an assumed modified gamma distribution (equation 9) for the precipitation drop size
 323 distribution. The three parameter are the shape factor μ , the median equivolumetric diameter D_0 ,
 324 and the normalized droplet concentration N_w :

$$n(D) = N_w f(\mu) \left(\frac{D}{D_0}\right)^\mu e^{\left[-\frac{(3.67+\mu)D}{D_0}\right]} \quad (9)$$

325 where D is diameter, and $f(\mu)$ is a function of μ

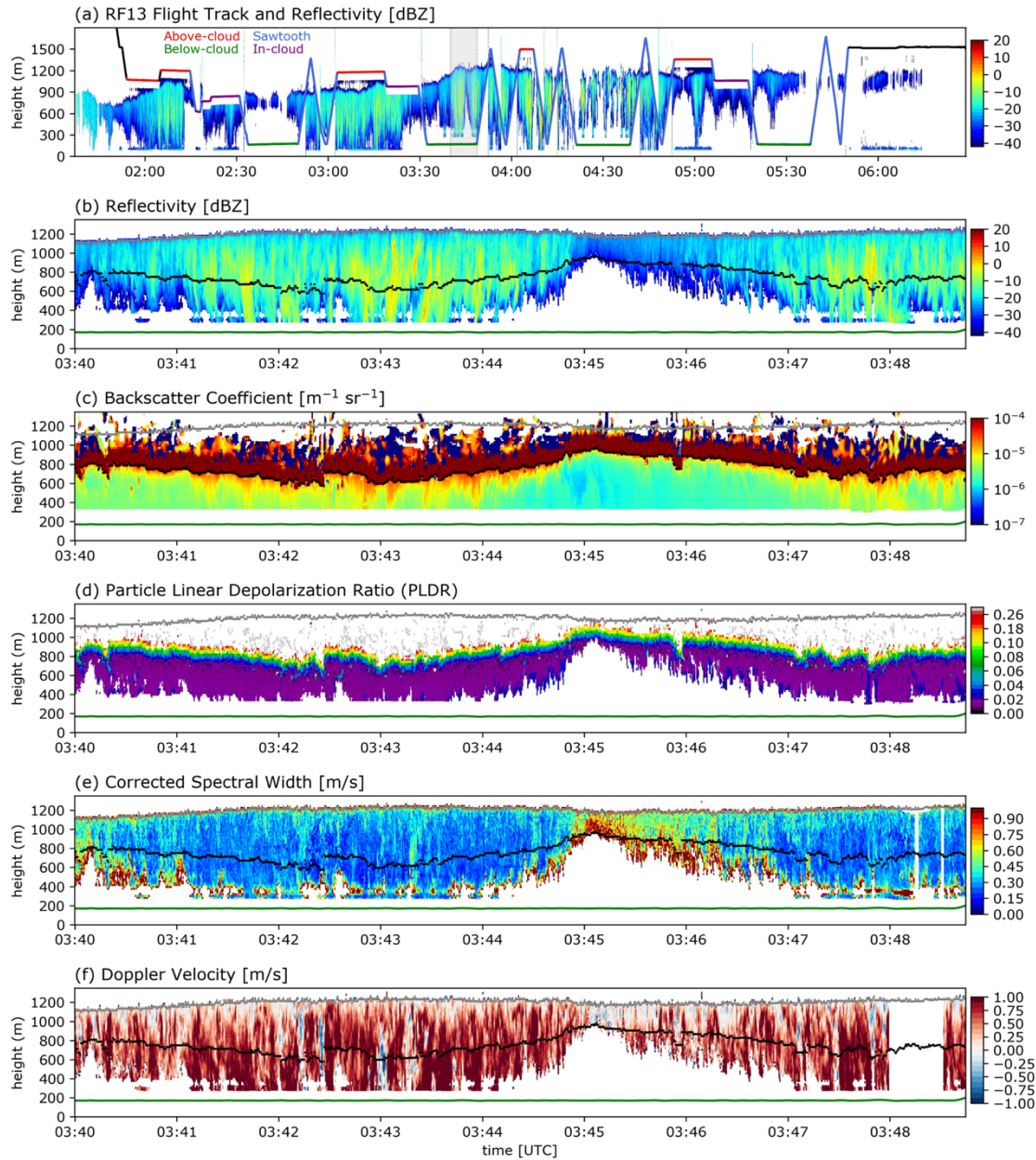
$$f(\mu) = \frac{6}{3.67^4} \frac{(3.67 + \mu)^4}{\Gamma(\mu + 4)} \quad (10)$$

326 where Γ is the gamma function. Integration of the droplet size distribution in (9) will yield the
 327 precipitation droplet number concentration, N_{precip} , as in equation 2.

328 Following O'Connor et al. (2005), one can show that for a fixed value of the shape factor, μ , the
 329 ratio of the radar reflectivity to lidar backscatter is proportional to the fourth power of the mean
 330 drop size, and the combination of radar reflectivity and lidar backscatter can therefore be used to
 331 calculate D_0 and N_w . In the retrieval algorithm, this is done assuming an initial value of $\mu = 0$.

332 The Doppler spectral width is then forward calculated and μ is increased or decreased in order to
333 match the observed Doppler spectral width (after applying corrections for beam width and
334 turbulent motions). The forward calculations require a model for the hydrometeor terminal fall
335 velocity, for which we use the model of Beard (1976). Once the three distribution parameters are
336 known, it is straightforward to calculate the rain rate, rain liquid water content, and mean rain drop
337 size, etc. using the fall velocity and equation (9). This retrieval technique has been widely used in
338 retrieving drizzle properties (e.g. Ghate & Cadetdu, 2019; Yang et al., 2018), including the CSET
339 campaign with airborne radar and lidar (Schwartz et al., 2019; Sarkar et al., 2021). Our
340 implementation largely follows O'Connor et al. (2005), except for estimation of the contribution
341 from air turbulence to the observed spectral width. Instead of using the horizontal wind speed to
342 estimate the length scale (we note O'Connor et al. (2005) originally developed the retrieval for
343 vertically pointing ground-based radar and lidar), we use the aircraft speed.

344 In addition to the radar-lidar retrieval technique, we also use a reflectivity-velocity (ZV) retrieval
345 technique (Frisch et al., 1995; Mace et al., 2002; Marchand et al., 2007). The first step in this
346 retrieval is to estimate the precipitation fall velocity from radar measured Doppler velocity, which
347 includes the effect of vertical air motions (i.e., updrafts/downdraft). We do this follow Orr and
348 Kropfli (1998) and partition the measured Doppler velocities into a set of height and reflectivity
349 bins (for each below-cloud zenith-pointing segment) and average the partitioned Doppler velocity
350 as an estimate for the fall velocity (as a function of height and radar reflectivity). The underlying
351 idea is that at a given altitude and reflectivity, there is a characteristic size distribution (with a
352 characteristic fall velocity) and by averaging the Doppler velocities over a narrow range of
353 reflectivity values, one averages out the effect of the updrafts and downdrafts leaving only the
354 mean fall velocity. In this study we use reflectivity bins are that 2 dBZ wide, and use 200 m vertical
355 bins with 100 m overlap. The results are not particularly sensitive to these choices, as long as there
356 is a healthy number of samples are available in each bin. Following Frisch et al. (1995), it is
357 straight-forward to obtain analytical expressions for distribution parameters D_0 and N_w given the
358 derived fall velocity, measured reflectivity, and an assumed shape factor μ . Except were stated
359 otherwise, we assume shape factor to be 0. One can show that the modified gamma distribution
360 (equation 9) reduces to the exponential distribution when the shape factor is zero. In the radar-
361 lidar retrieval we find retrieved shape factor is often quite small and we will examine and discuss
362 the sensitivity of the ZV retrieval to assumed shape factor values in Section 4.2.



363

364 **Figure 1.** Example radar and lidar data collected during the SOCRATES. Panel a shows the flight
 365 tracks and reflectivity fields from research flight 13 (RF13), with different segments color-coded
 366 as in Figure S1. The grey shading marks a portion of one below-cloud level leg, and a zoom-in
 367 view of the radar and lidar fields for this segment are shown in panels b-f: (b) radar reflectivity;
 368 (c) lidar backscatter coefficient; (d) lidar particle linear depolarization ratio; (e) radar spectral
 369 width; (f) radar doppler velocity. The grey lines show the estimated cloud top, the black lines show
 370 the estimated cloud base, and the green line shows the location of the aircraft.
 371

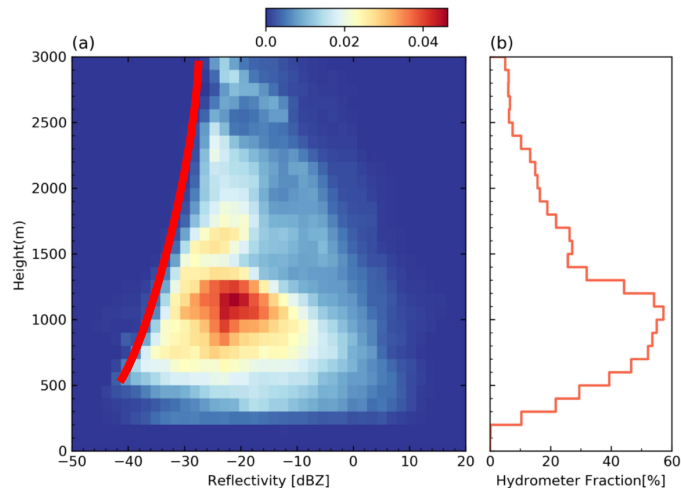
372 3 Campaign overview

373 To get a general sense of the hydrometers (clouds and precipitation) sampled by the airborne W-
374 band radar during the SOCRATES, Figure 2a shows the joint histogram of radar reflectivity with
375 height observed during below-cloud, zenith-pointing periods (i.e. as illustrated in Figure S1).
376 Here the histogram is normalized by the number of radar columns, such that the value in each bin
377 indicates how often hydrometers (cloud and precipitation) have a reflectivity (with +/- 1 dBZ of
378 the given value) in the given altitude/height range; and the sum at each height (row) will give the
379 hydrometer fraction (Figure 2b).

380 Note that there is no data to the left of the red line in panel a. This is because of limited radar
381 sensitivity, and as distance increases, the minimum detectable reflectivity value increases. Likewise,
382 there are no data from 0 to 200 meters altitude because the aircraft lowest legs were typically flown
383 at around 100-150 m altitude, and the radar blanking interrupt (the region corresponding to the
384 time when the radar outgoing pulse is being, or has just been, transmitted and the radar system has
385 not yet begun measuring the return power) typically extends about 203 m above this (Schwartz et
386 al., 2019).

387 The maximum frequency of hydrometers observed by the radar occurred between 700 and 1200
388 meters, with a hydrometer fraction over 50%. (Note this is not projected area or the fraction of
389 radar columns with a significant echo at any altitude, that value is near 90%). Reflectivity factors
390 larger than -10 dBZ are relatively rare and there is no distinct mode associated with precipitation
391 (that is, no peak with a reflectivity larger than about -20 dBZ). Reflectivity factors larger than -10
392 dBZ are common of the Southern Ocean (see for example Mace and Protat 2018), but such factors
393 are associated with fronts or convection (including the shallow convection sometimes associated
394 with vigorous open cells) and not typical of the shallow (cloud tops < 2 km) and largely overcast
395 stratocumulus sampled during SOCRATES. Rather there is a single mode or continuum of
396 reflectivity that span reflectivity factors from about -40 dBZ (where there are few if any
397 precipitation sized particles) to values around -10 dBZ (where precipitation is still light with rain
398 rate < 1 mm hr⁻¹ but can have a substantial impact on cloud condensation nuclei and cloud lifetime,
399 Kang et al., 2022) and a peak below -20 dBZ. Most of this cloud is supercooled. Overall, we find
400 that about 80% of the stratocumulus sampled during SOCRATES had a cloud top temperature <
401 0°C and cloud depth < 600m (figure not shown), and about 62% of the stratocumulus were
402 precipitating, defined as 3 consecutive radar bins (about 60 meters) below cloud base with a
403 reflectivity greater than -40dBZ. The occurrence of precipitation drops to 34% if a reflectivity
404 threshold of -20 dBZ is applied (in spite of the detections being below cloud base), indicative of
405 very light nature of the precipitation.

406

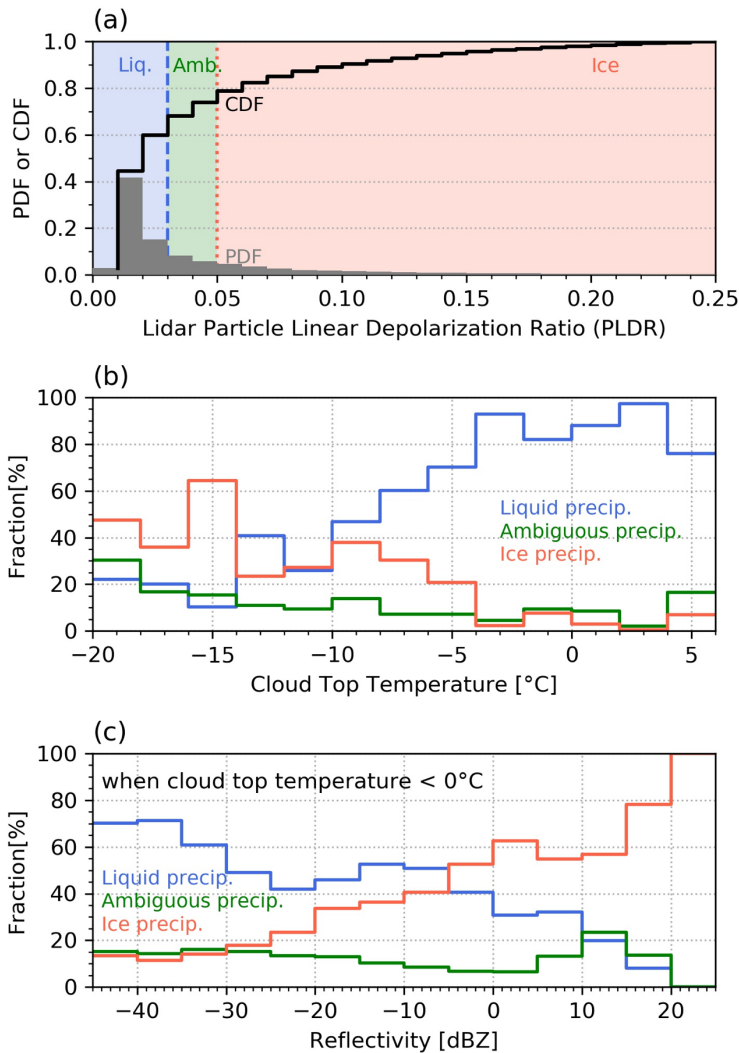


407
 408 **Figure 2.** (a) Joint histogram of hydrometer (cloud & precipitation) radar reflectivity with height
 409 observed by the airborne W-band radar during below-cloud, zenith-pointing periods (i.e., when
 410 aircraft is flying below the cloud, as illustrated in Figure S1). Histogram is normalized by total
 411 number of radar “columns” such that the histogram values is the fractional occurrence (see text).
 412 (b) hydrometer fraction [%] at each height of all radar “columns”. The red line on panel a shows
 413 the minimum detectable reflectivity values by HCR as a function of height.

414 What is the phase of the precipitation sampled during the SOCRATES? As described in Section
 415 2.3.2, we determine the precipitation phase using the lidar particle linear depolarization ratio
 416 PLDR (Figure 1d), and interpret the precipitation as liquid phase when $PLDR < 0.03$; ice phase
 417 when $PLDR > 0.05$; and ambiguous for PLDR values in between. Figure 3a shows that around
 418 60% of the precipitation from the zenith-pointing segments are liquid phase and about 20% of the
 419 precipitation are ice phase, with the remaining 20% being ambiguous phase. How does
 420 precipitation phase relate to the cloud top temperature? Figure 3b shows the relative occurrence of
 421 precipitation in difference phases as a function of cloud top temperature (CTT). For the warm-
 422 topped clouds ($CTT > 0^{\circ}\text{C}$), we expect that all the precipitation should be liquid phase.
 423 Temperature is not used in the phase retrieval, and consistent with the discussion in Section 2, the
 424 low occurrence of ambiguous or ice phase precipitation with $CTT > 0^{\circ}\text{C}$ is indicative of the low
 425 retrieval error. For the cold-topped clouds ($CTT < 0^{\circ}\text{C}$), liquid precipitations still dominate for
 426 clouds with CTT between 0 and -10°C , with the ice fraction increasing as temperature decreases.
 427 But it is not until about a CTT of -15°C that ice phase appears to dominate. It could be that the
 428 apparent peak in ice phase occurrence near -15°C is a result of dendric growth (or secondary ice
 429 product associated with dendrites), as dendric growth is known to occur near this temperature (e.g.,
 430 von Terzi et al., 2022) but there is too little data here to be confident this uptick in ice phase is
 431 statistically significant.

432 An interesting question related to phase is whether or not precipitation phase is related to radar
 433 reflectivity. Zhang et al. (2017) have shown that lidar depolarization ratios is correlated with radar
 434 reflectivity, and for the SO in particular, Mace and Protat (2018) show that W-band radar
 435 reflectivity greater than -10 dBZ is associated with ice-phase hydrometeors (based on
 436 CAPRICORN observations). Figure 3c shows the occurrence of the different precipitation phase
 437 for cold-topped clouds as a function of reflectivity. Overall, it shows that reflectivity factors less

438 than about -10 dBZ are predominately liquid, while reflectivity factors greater than 0 dBZ is
 439 predominately ice. We will discuss this result in more detail in the conclusions.
 440



441 **Figure 3.** (a) Probability and cumulative density functions for lidar particle linear depolarization
 442 ratio (PLDR) for below-cloud precipitation (b) The fraction of liquid, ice, and ambiguous
 443 precipitation as a function of cloud top temperature. (c) The fraction of liquid, ice, and
 444 ambiguous precipitation as a function of radar reflectivity. To distinguish different precipitation
 445 type, liquid precipitation is marked as blue, ice precipitation is marked as red, and ambiguous
 446 precipitation is marked as green.
 447

448

449 **4 Precipitation Retrievals**

450 In this section, we will explore a hierarchy of retrieval methods based on complexity, from (1) the
 451 simplest Z-R relationship approach where only one variable reflectivity Z is known, to (2) a ZV
 452 retrieval using two variables (reflectivity Z and Doppler velocity V), to (3) a radar-lidar retrievals
 453 based on three variables (reflectivity radar reflectivity Z, doppler spectral width σ_d , and lidar

454 backscatter β). In section 4.1, we will develop Z-R relationships based on in situ data. In section
455 4.2, we will demonstrate the results from ZV and radar-lidar liquid precipitation retrievals using a
456 case example, and in section 4.3, we evaluate these retrievals using in-situ aircraft observations
457 from all the segments where retrievals were performed.

458 4.1 Reflectivity to rain rate (Z-R) relationships

459 One objective of this study is to estimate Z-R relationships of the form $Z = aR^b$. Z-R relationships
460 are useful and convenient, requiring only one independent variable (reflectivity Z) to estimate rain
461 rate R . Such relationships have a long history in atmospheric science, and as concerns
462 stratocumulus in particular, relationships have been derived in past studies for stratocumulus over
463 the Eastern Pacific (Comstock et al., 2004), over the north-east Atlantic and in U.K. coastal waters
464 (Wood, 2005), and for nocturnal stratocumulus clouds off the California Coast (VanZanten et al.,
465 2005). More recently, Protat et al. (2019b) estimated Z-R relationships at the surface over the
466 global ocean, including the Southern Ocean, based on surface disdrometer measurements. In this
467 section, we will derive Z-R relationships using SOCRATES aircraft observations following the
468 method presented in Section 2.2.3 and compare our results with previous studies.

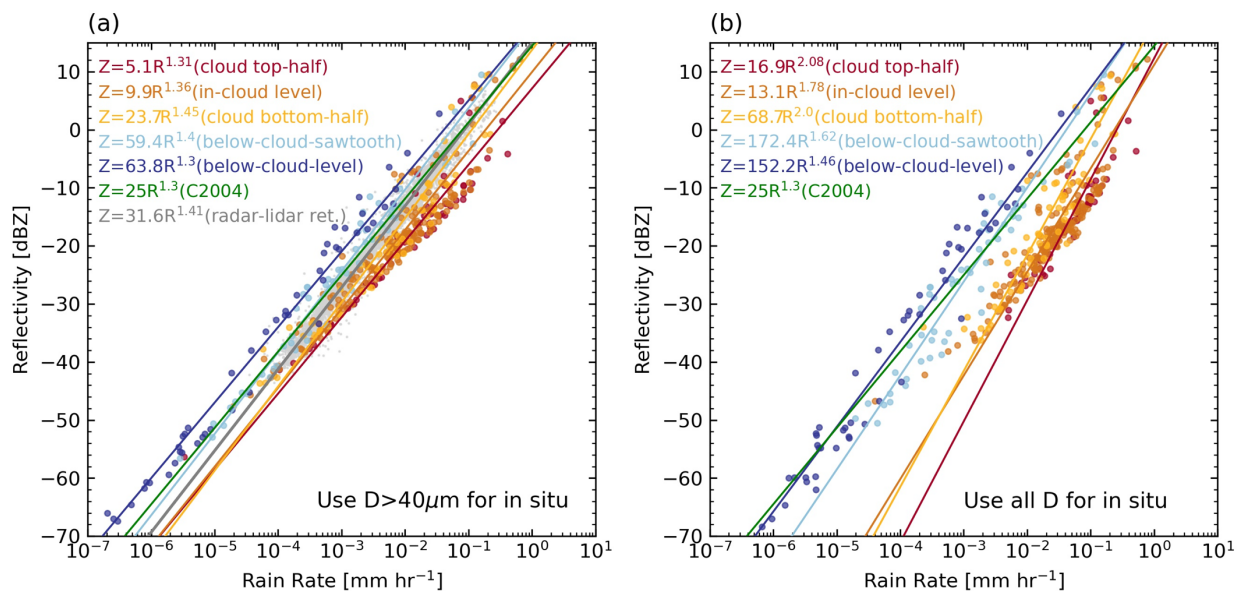
469 Figure 4 shows the Z-R relationships derived using in situ data taken at different locations relative
470 to the cloud layer and surface (see Figure S1 for a schematic). Table 2 lists the corresponding a
471 and b coefficients. In Figure 4a, we only consider droplets with a diameter larger than $40\ \mu\text{m}$
472 following Comstock et al. (2004), while in Figure 4b, we include all droplets including those
473 droplets with a diameter smaller than $40\ \mu\text{m}$. We will focus on Figure 4a first. Figure 4a shows
474 that estimated Z-R relationships do have a vertical dependence. The intercept controlled by
475 coefficient a increases as one moves from the cloud layer to the surface, while the slope controlled
476 by exponent b remains largely unchanged. The vertical dependence of Z-R was also noticed in
477 previous studies (e.g. Comstock et al., 2004; vanZanten et al., 2005). The exponent b estimated in
478 Figure 4a ranges from 1.3 to 1.45, with a (one sigma) uncertainty that ranges from 0.5 to about 0.1,
479 based on a bootstrap resampling technique (uncertainties are listed in Table 2). Note the
480 uncertainties in the a and b coefficients are not independent, but rather are positively correlated
481 such that a larger estimate for the a -value is associated with a larger estimate for the b -values.
482 Table 2 also lists some Z-R relationships estimated from other studies mentioned above. Overall,
483 we find the exponent b to be similar to that from Comstock et al. (2004), vanZanten et al. (2005),
484 and many other earlier studies summarized in Rosenfeld and Ulbrich (2003) over other regions
485 and other cloud types. Later in this section we will compare the rain rate derived from Z-R
486 relationships with rain rate derived from two other retrieval methods.

487 The above analysis is based on the idea that only droplets larger than $40\ \mu\text{m}$ are considered
488 precipitation. But droplets smaller than $40\ \mu\text{m}$ can and do contribute to the flux of liquid water
489 (Nicholls, 1984). What happens if small droplets with a diameter smaller than $40\ \mu\text{m}$ are included
490 when calculating Z and R from in situ DSDs? The results are shown in Figure 4b. Comparing
491 Figure 4a and 4b, one can see that the estimated Z-R relationships is very sensitive to whether one
492 excludes smaller drops, especially for the data collected in the cloud. Differences in the estimated
493 Z-R are less dramatic when using in situ data outside of the cloud (i.e. below-cloud portion of the
494 sawtooth leg and below-cloud level legs).

495 To explore the importance of the smaller droplets, Figure 5a shows an example of DSDs measured
 496 near the top of a cloud, near the bottom cloud and below cloud during one sawtooth leg, as well as
 497 a nearby below-cloud level leg (depicted in the bottom panel). The associated liquid water flux
 498 distribution $D^3N(D)V(D)$ is shown Figure 5b, and the reflectivity distribution $D^6N(D)$ in Figure
 499 5c. Note as in the microphysical retrievals, here we use the terminal fall velocity model of Beard
 500 (1976) for $V(D)$. Below-cloud, small droplets evaporate much more quickly than larger droplets,
 501 and most of the contributions to the liquid water flux comes from larger droplets, such that the
 502 effect of small droplets on liquid water flux and reflectivity can be largely neglected. We hasten
 503 to add, however, this is true not true for the total number concentration (Figure 5a); where small
 504 droplets remain more numerous (than droplets above $40\ \mu\text{m}$), and includes many particles with
 505 sizes smaller than $5\ \mu\text{m}$, which one might consider haze-particles or hydrated-aerosols rather than
 506 cloud droplets. Within the cloud layer, small droplets make a large contribution to the liquid water
 507 flux and contribute slightly to the reflectivity. Droplets in the diameter range of $10\text{-}40\ \mu\text{m}$
 508 contribute 78% of the liquid water flux in the top half of the cloud, and still comprise about half
 509 of the water flux in the bottom half of the cloud. Contributions to the reflectivity from droplets in
 510 the range of $10\text{-}40\ \mu\text{m}$ are smaller than those of larger droplets, but both make a non-trivial
 511 contribution.

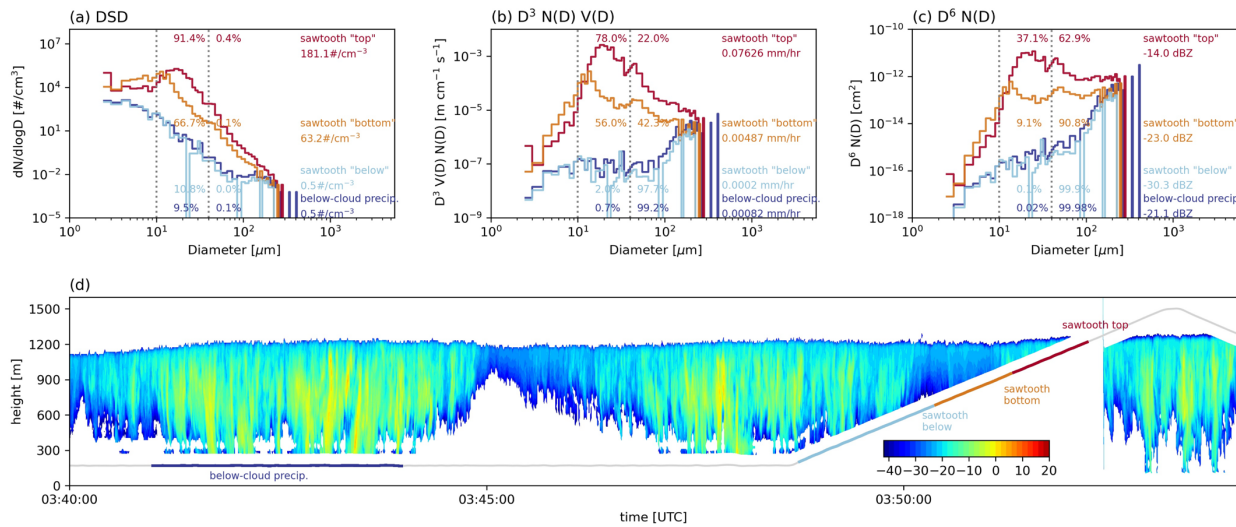
512 In short, as Figure 5 and the differences in estimated Z-R in Figure 4a and Figure 4b highlight, the
 513 sedimentation of small droplets is (or can be) a significant component of the total liquid water flux
 514 in cloud and applying the Z-R relationship derived from only larger particles or from below-cloud
 515 measurements effectively ignores the contribution from small particles (and below-cloud Z-R
 516 equations should be applied with caution to in-cloud reflectivity measurements and should be
 517 expected to underestimate the total liquid water flux).

518
 519
 520



521
 522 **Figure 4.** Z-R relationship derived using in situ data and retrievals. Diameter $>40\ \mu\text{m}$ cutoff for
 523 the in situ measurements is imposed in panel a, while panel b does not apply any cutoff, and
 524 considers all droplet sizes for in situ data.

525
526
527



528
529
530
531
532
533
534
535
536
537
538
539
540
541
542
543
544
545
546
547
548
549
550
551
552
553
554
555
556
557

Figure 5. Example case to show the contributions of droplets in different size ranges with in situ measurements taken from different segments: (a) average droplet size distribution; (b) product of diameter cubed, droplet size distribution and terminal fall velocity; (c) product of diameter to the power of six and droplet size distribution; (d) reflectivity field and flight track for this example, the color-coded lines marked the locations of different segments showing in panel a-c. The vertical dashed line in panels a-c is the reference line for 10 μ m and 40 μ m. The percentage on panel a, b, and c show the contributions from different size range to droplet number concentration, to rain rate, and to reflectivity, respectively.

558 Table 2. Z-R relationship of the form $Z = aR^b$

| Equation | Location | Remarks | Reference |
|---|---|---|-------------------------|
| $Z = (5.1 \pm 3.5) R^{(1.31 \pm 0.1)}$ [$Z = (16.9 \pm 26.1) R^{(2.08 \pm 0.25)}$] | the top half of the cloud layer from the sawtooth leg | Estimated using SOCRATES aircraft in situ measurements with and without the 40 μ m cutoff, [without given in brackets] | This study |
| $Z = (9.9 \pm 2.8) R^{(1.36 \pm 0.05)}$ [$Z = (13.1 \pm 6.8) R^{(1.78 \pm 0.11)}$] | in-cloud level legs | | |
| $Z = (23.7 \pm 11.6) R^{(1.45 \pm 0.08)}$ [$Z = (68.7 \pm 68.5) R^{(2.0 \pm 0.16)}$] | bottom half of the cloud layer from the sawtooth leg | | |
| $Z = (59.4 \pm 21.4) R^{(1.4 \pm 0.04)}$ [$Z = (172.4 \pm 106.7) R^{(1.62 \pm 0.06)}$] | the below-cloud portion of the sawtooth leg | | |
| $Z = (63.8 \pm 47.1) R^{(1.3 \pm 0.05)}$ [$Z = (152.2 \pm 277.9) R^{(1.46 \pm 0.09)}$] | below-cloud level legs. | | |
| $Z = (31.6 \pm 1.4) R^{(1.41 \pm 0.007)}$ | Cloud base | Estimated using SOCRATES W-band radar measured reflectivity and radar-lidar retrieved rain rate just-below cloud base | |
| $Z = 25R^{1.3}$ | Cloud base | Estimated for stratocumulus over Eastern Pacific | Comstock et al. (2004) |
| $Z = 12.92 R^{1.47}$ | Cloud base | Estimated using aircraft in situ DSD measurements for nocturnal stratocumulus clouds over California Coast | vanZanten et al. (2005) |
| $Z = 12.5 R^{1.18}$ | All in-cloud levels | Estimated using aircraft in situ DSD measurements for stratocumulus over the north-east Atlantic and in U.K. coastal waters | Wood (2005) |

559 Note: here uncertainty is estimated using either by bootstrapping (rows 1-5) or moving block
 560 bootstrapping (row 6) with the one-sigma uncertainty given after the plus-minus sign. For the Z-R
 561 relationship that is estimated using in situ measurements, the Z-R relationship estimated using only larger

562 droplets, with a diameter greater than $40\mu\text{m}$, is listed first, followed by the Z-R relationship estimated
 563 using all droplets included those droplets with a diameter smaller than $40\mu\text{m}$. For the equations above,
 564 the reflectivity Z is in the unit of $\text{mm}^6\text{mm}^{-3}$, and the rain rate is in the unit of mm hr^{-1} . For the equations in
 565 the past studies with the form of $R = cZ^d$ or have different units, we rearranged the equation and
 566 converted the units to keep the consistency and make it easier to compare. Unless noted, the default band
 567 for reflectivity is W-band.

568 4.2 ZV retrieval and radar-lidar retrieval

569 In this subsection, we examine both the ZV retrieval and radar-lidar retrievals using the zenith-
 570 pointing remote sensing data collected when the aircraft was flying level-legs below the cloud. We
 571 will begin with one case study, compare results from different retrieval methods, and then examine
 572 the sensitivity of ZV retrieval results to the assumed shape factor μ . The overall retrieval
 573 performance will be evaluated in Section 4.3.

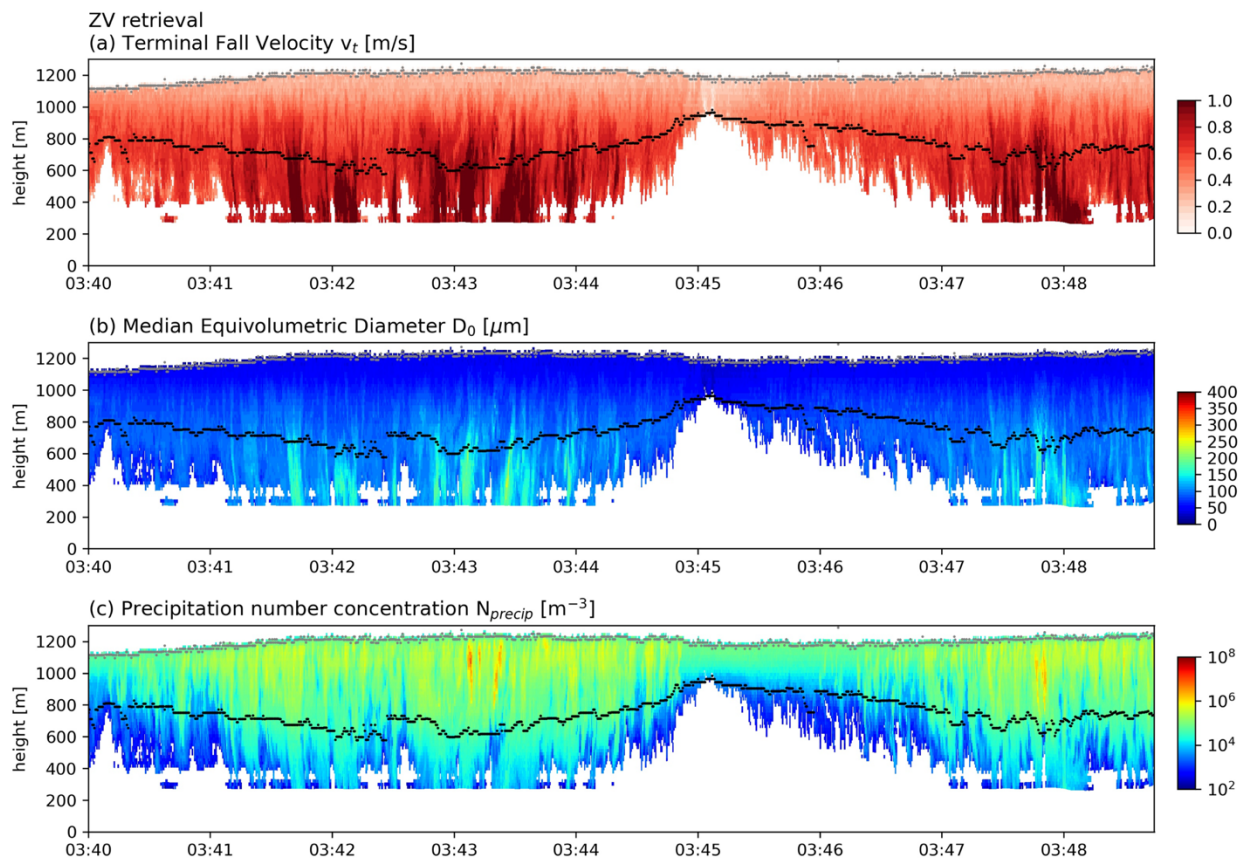
574 Applying the ZV retrieval (described in Section 2.3.3) to the example presented in Figure 1, the
 575 parameters D_0 and N_{precip} can be derived from measured reflectivity Z , assumed shape factor μ , and
 576 derived terminal fall velocity. Figure 6a shows the reflectivity-weighted terminal fall velocity, v_t ,
 577 derived following Orr and Kropfli (1998). Here we see generally larger v_t toward the bottom of
 578 the cloud, and in precipitation shafts (regions of relatively high reflectivity extending below cloud
 579 base). Figure 6b and 6c shows derived median equivolumetric diameter D_0 , and precipitation
 580 concentration N_{precip} , assuming $\mu = 0$. Not surprisingly, Figure 6b shows that D_0 is larger where v_t
 581 is larger, and is about $100\text{-}200\mu\text{m}$ below cloud base. Figure 6c shows N_{precip} below cloud base is
 582 in the order of $10^3\text{-}10^5\text{ m}^{-3}$.

583 Applying the radar-lidar retrieval technique to the example presented in Figure 1, with three input
 584 variables (radar reflectivity Z , doppler spectral with σ_d , and backscatter coefficient β), we can also
 585 solve for shape factor μ , median equivolumetric diameter D_0 , and precipitation number
 586 concentration N_{precip} , as shown in Figure 7. The shape factor μ describes the shape of the DSD
 587 (equation 9) and larger μ implies narrower distributions. As in O'Connor et al. (2005), we find
 588 large areas with broad DSDs (small μ). Narrow DSDs implied by large μ are typically found
 589 underneath the thicker portion of the clouds (and as we will see later have larger rain rates). The
 590 median equivolumetric diameter D_0 is mostly between $50\text{-}250\mu\text{m}$, with larger sizes occurring
 591 where μ is larger. Again, this is similar to what O'Connor et al. (2005) observed and appears to
 592 be quite typical for drizzling stratocumulus. Comparing the two retrieval methods, both D_0 and
 593 N_{precip} from ZV retrieval (Figure 6) tend to be more spatially homogeneous below cloud base than
 594 that from radar-lidar retrieval (Figure 7), and the D_0 from ZV retrieval tends to be smaller than that
 595 from radar-lidar retrieval in the precipitation shafts (where the assumption of a small value for the
 596 shape factor appears problematic, more on this below).

597 Once the parameters that determine the DSDs are derived, it is straightforward to calculate other
 598 precipitation properties such as rain rate. Figure 8b and c show the ZV retrieved the rain rate
 599 (assuming $\mu = 0$) and radar-lidar retrieval retrieved the rain rate. Overall, the two retrieval methods
 600 give similar results (mean of rain rate from ZV retrieval is 0.0096 mm hr^{-1} , and mean of rain rate
 601 from radar-lidar retrieval is 0.0093 mm hr^{-1}). With derived Z-R relationships from section 4.1, one
 602 can also derive rain rate by apply them to the radar reflectivity fields, as shown in Figure 8a, with
 603 derived rain rate by applying Z-R relationships shown in Figure 4a from sawtooth-top to the top

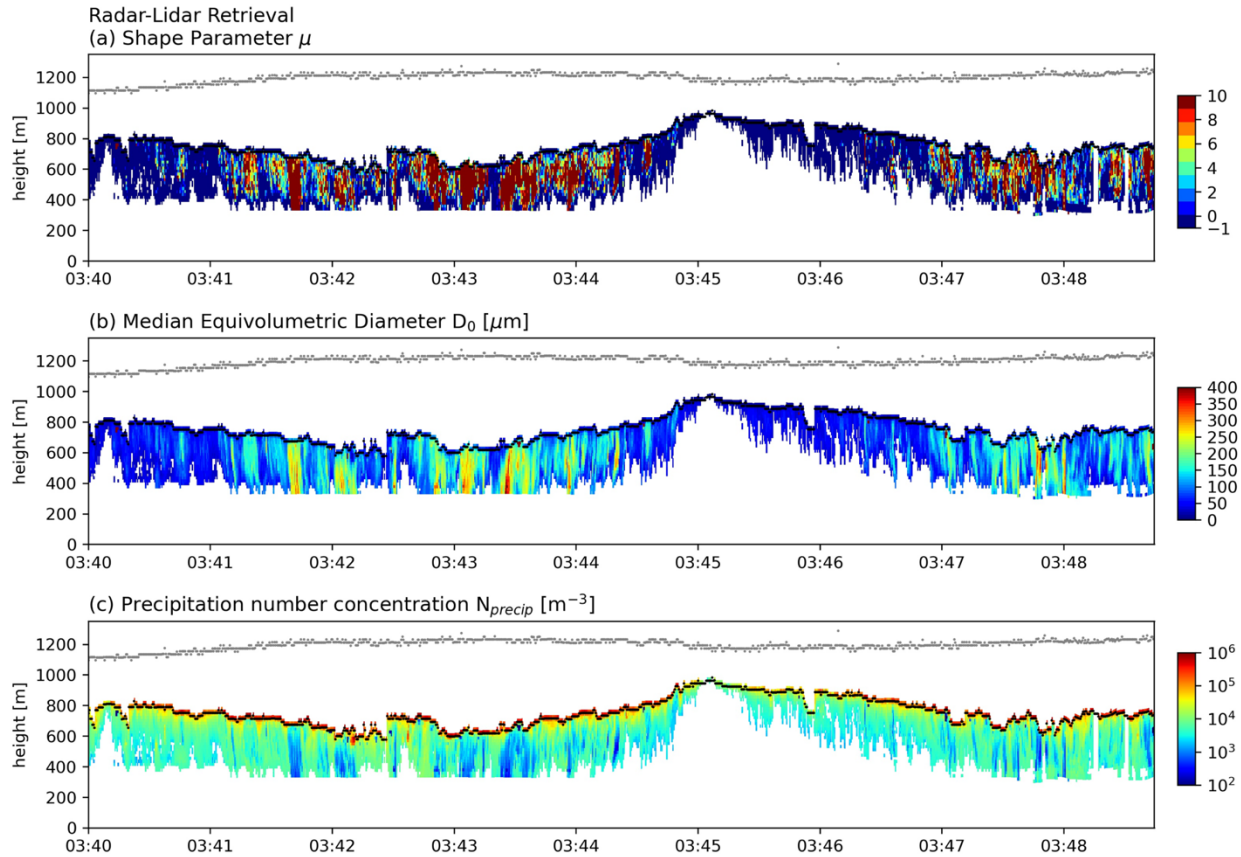
604 half of the cloud, from sawtooth-bottom to the bottom half of the cloud; as well as sawtooth-below
 605 to area below the cloud base. Overall, the retrieved rain rate has a magnitude that is around 0.001-
 606 0.1 mm hr⁻¹. The discontinuity in the rain rate fields in Figure 8a is because three different Z-R
 607 relationships are applied to different regions. The difference in Z-R relationships (i.e. with or
 608 without D>40 μm cutoff) also results in differences in derived rain rate (Figure S7), especially for
 609 the in-cloud portion. Overall, regardless of the retrieval approaches, it can also be seen that higher
 610 rain rates tend to occur below the geometrically thicker portion of the clouds, and we will explore
 611 the scaling between rain rate and cloud depth further in Section 6.

612 In Figures 6 and Figure 8b, we assume $\mu = 0$ in the ZV retrieval, while retrieved μ from radar-lidar
 613 retrieval clearly shows spatial variations (Figure 7a). How will ZV retrieved D_0 , N_{precip} , and rain
 614 rate vary with assumed μ ? Figure S8 shows that the derived D_0 increases with increasing μ values
 615 such that mean D_0 just below cloud base is 102 μm when $\mu = 0$, and is 156 μm when $\mu = 10$. In
 616 contrast, as shown in Figure S9, the derived N_{precip} decreases significantly with increasing μ values,
 617 with mean N_{precip} at cloud base is about $1.2 \times 10^5 \text{ m}^{-3}$ when $\mu = 0$, and is $1.2 \times 10^3 \text{ m}^{-3}$ when $\mu =$
 618 10. However the derived rain rate (Figure S10) shows relatively little dependence on assumed μ ,
 619 with rain rate at cloud base decrease slightly from about 0.009 mm hr⁻¹ ($\mu = 0$) to about 0.007
 620 mm hr⁻¹ ($\mu = 10$). The small sensitivity in rain rate ultimately arises because the liquid water flux
 621 is to first order given by the velocity (which is input to the retrieval) times the liquid water content
 622 (which is strongly constrained by the reflectivity that is likewise input to the retrieval).
 623

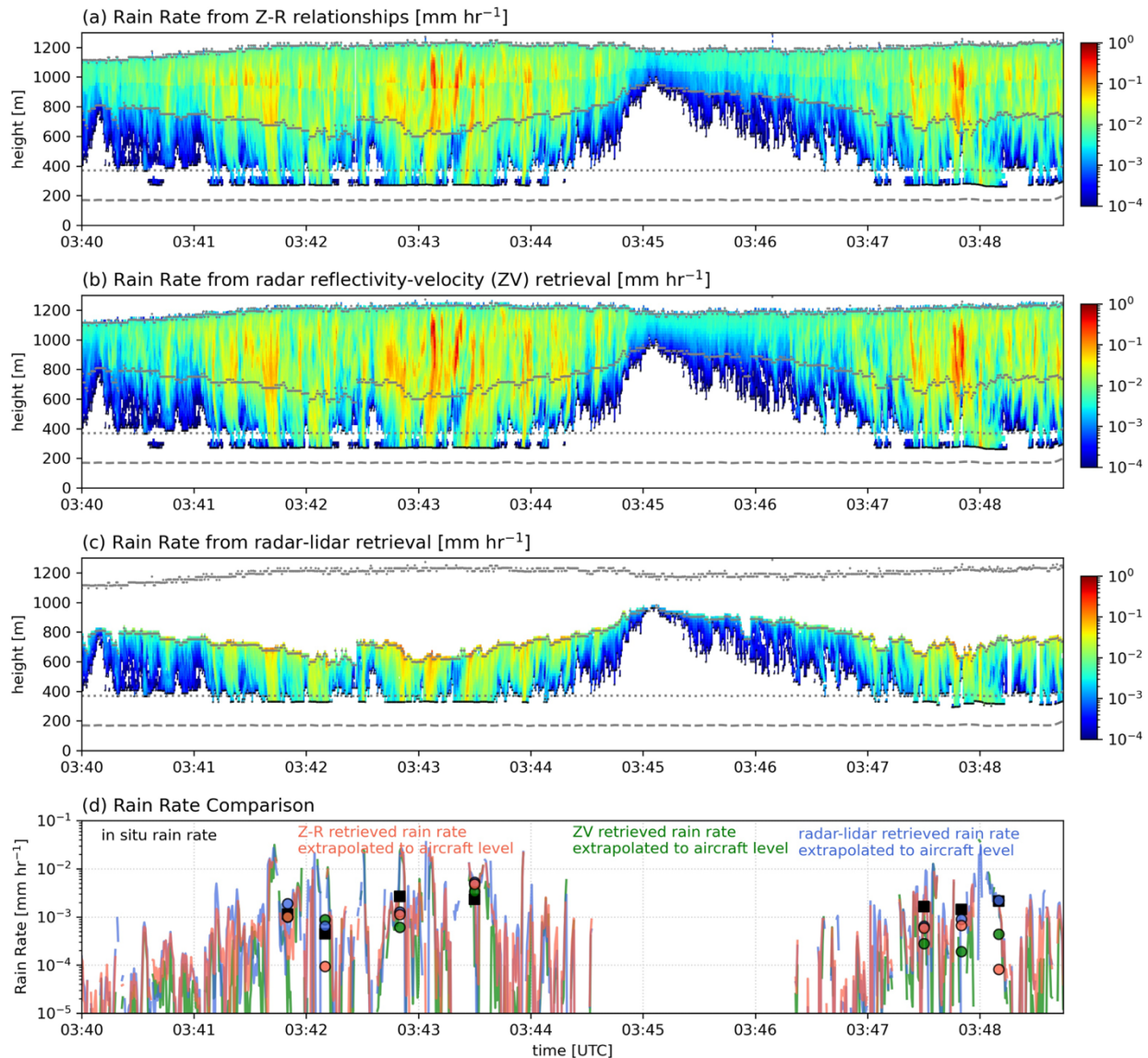


624
 625 **Figure 6.** A time-height plot of ZV method retrieved drizzle properties assuming shape factor
 626 for the example segment is shown in Figure 1. (a) reflectivity-weighted the terminal fall velocity

627 v_i ; (b) median equivolumetric diameter D_0 , and (c) precipitation number concentration N_{precip} .
 628 The grey lines show the estimated cloud top, the black lines show the estimated cloud base.
 629
 630



631
 632 **Figure 7.** A time-height plot of radar-lidar retrieved drizzle properties for the example segment is
 633 shown in Figure 1. Radar-lidar retrieval method derived parameters for modified gamma
 634 distribution (a) shape factor μ ; (b) median equivolumetric diameter D_0 , and (c) precipitation
 635 number concentration N_{precip} . The grey lines show the estimated cloud top, the black lines show
 636 the estimated cloud base.
 637



638
 639 **Figure 8.** Retrieved rain rate for example case using (a) Z-R relationships ($D > 40\mu\text{m}$), (b) ZV
 640 retrieval technique, and (c) radar-lidar retrieval technique, and (d) their comparisons with in situ
 641 estimates. In panels a-c, the dashed grey line shows the location of the aircraft, while the dotted
 642 line is a reference line to show 200 meters above the aircraft's location. In panel d the retrieved
 643 rain rates were extrapolated to the aircraft level to compare with the in situ data. The pink line
 644 shows the rain rate retrieved with Z-R relationships, the green line shows the rain rate retrieved
 645 with the ZV retrieval technique, and blue line shows the rain rate retrieved with the radar-lidar
 646 retrieval technique. The black squares represent the rain rate estimated with in situ
 647 measurements, where rain rates are derived from averaged droplet size distribution (merged CDP
 648 and 2DS) over 20 seconds. Over that same time window, the median value of the retrieved rain
 649 rate time series was taken, denoted as pink dots (Z-R relationship), green dots (ZV retrieval) and
 650 blue dots (radar-lidar retrieval).
 651

652 4.3 Retrieval validation

653 How good are the rain rate retrievals? One would think a simple comparison between the retrieved
654 rain rate with in situ measurements from the aircraft could answer this question. But there are a
655 few challenges that need to be overcome.

656 The first challenge is that retrieved rain rates that are closest to the aircraft level marked as a dashed
657 line around 200 m in Figure 8) are still at least 150 meters away, making it difficult to make a
658 direct comparison. This is because there is a blanking interrupt, a brief period where one needs to
659 wait for the outgoing pulse to exit the radar (or lidar) system and for the effect of strong scattering
660 from nearby objects (clutter) to dissipate. To overcome this difficulty, we extrapolate the retrieved
661 rain rate downwards to the aircraft level by fitting an exponential function to each radar column.
662 The assumption is that the rain rate varies with distance below the cloud base exponentially due to
663 evaporation (Wood, 2005; Comstock et al., 2004). Figure S11 in the supporting information shows
664 an example of rain rate derived from the exponential fit, and demonstrates that the exponentially
665 fitted rain rate shows reasonable agreement with the retrieved rain rate where such is retrieved.
666 Figure 8d compares the extrapolated rain rate from the Z-R relationship (red line), extrapolated
667 rain rate from ZV retrieval (green line), extrapolated rain rate from radar-lidar retrieval (blue line).
668 To further increase our confidence, we only compare the extrapolated rain rate from those periods
669 where the original retrieved rain rate extends to within 200m of the aircraft (i.e. when the rain
670 extends down to dotted reference line). Another challenge is the limited sampling volume of the
671 in situ probes. To overcome this difficulty, we average the in situ DSD over a 20s period, marked
672 as black squares in Figure 8d, and similarly, we also average the corresponding retrievals over the
673 same 20s time window, marked by the red, green and blue dots. It can be seen that the retrieved
674 rain rate shows reasonable agreement with in situ data for this case.

675 We repeated this analysis for the liquid-precipitation retrievals for all the SOCRATES flights and
676 summarize the results in Figure 9. Overall, the Z-R, ZV, and radar-lidar retrievals compare well
677 with the in situ, with Pearson correlation coefficient of 0.83, 0.88 and 0.68, respectively. Despite
678 the simplicity of the approach, even the rain rate derived from Z-R relationship shows good
679 performance compared to the in situ values, with a fractional difference (difference in 20s medians
680 / average of 20s medians) of only -8.0%. If we estimate the uncertainty in the retrieved rain rate
681 via error propagation, and we estimated the uncertainty in reflectivity as 1.5 dB for reflectivity
682 (following O'Connor et al., 2005) and 10% for lidar backscatter (e.g., Schwartz et al., 2019), we
683 estimate the uncertainty in the radar-lidar retrieved rain rate would be 18%. Similarly, with the
684 uncertainty of 1.5 dB for reflectivity, and 10% uncertainty for terminal fall velocity (see Tansey
685 et al., 2022), we estimate the uncertainty in the ZV retrieved rain rate to be 44%. As for the Z-R
686 relationship (using the below-cloud sawtooth leg relationship), the estimated the uncertainty in
687 rain rate is 38.4%. Relative to the expected uncertainties due simply from uncertainties in the
688 inputs, all three retrievals compare well with the in situ data.

689

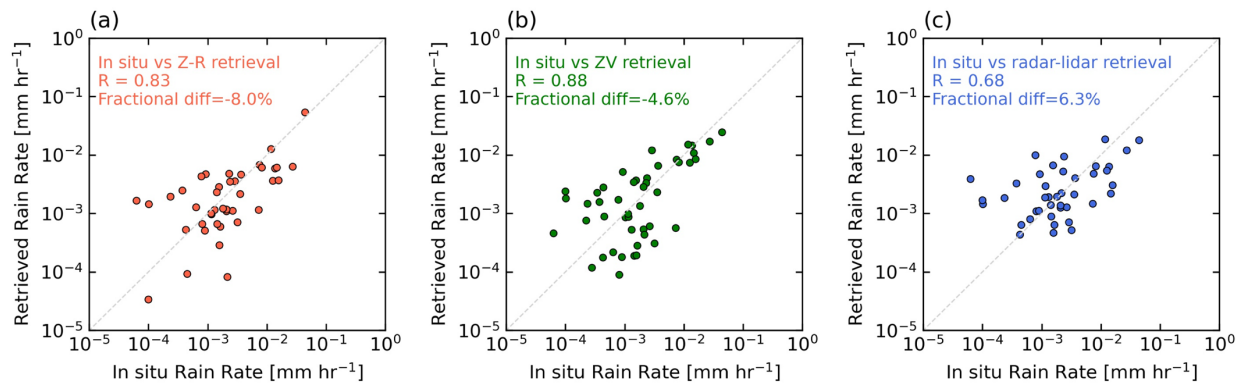
690

691

692

693

694
695
696



697
698 **Figure 9.** Comparison of in situ estimates with (a) Z-R retrieval, (b) ZV retrieval, and (c) radar-
699 lidar retrieval for the entire campaign. The retrieved rain rates plotted here that were extrapolated
700 to the aircraft level (see Figure 8, S11) to compare with the in situ data. Fractional difference is
701 calculated as the difference between the retrieved and in situ median value divided by the
702 average of the medians.
703

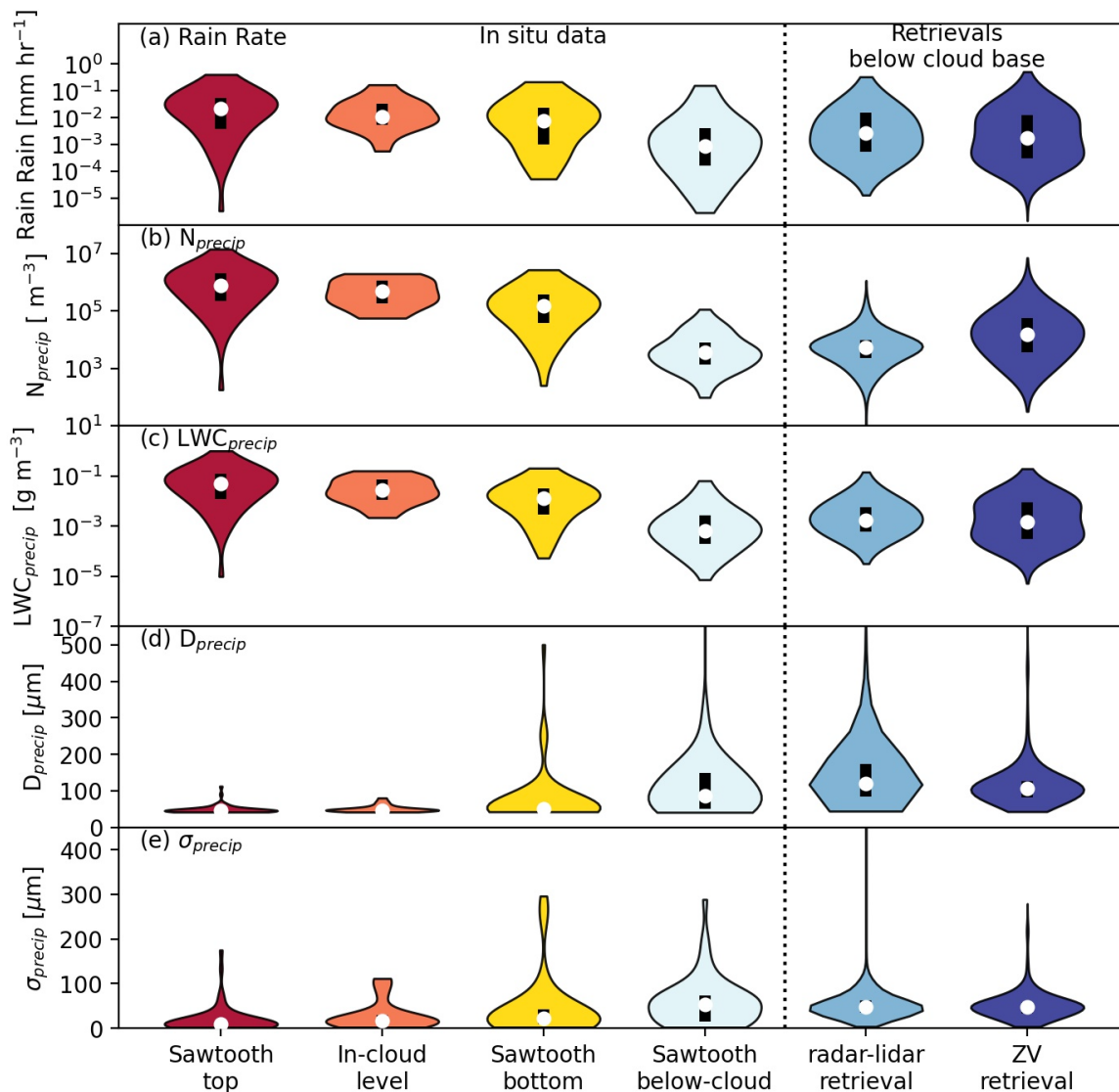
704 5 Vertical distribution of precipitation properties

705 In this section, we will apply the precipitation observations and retrievals to study the vertical
706 distribution of precipitation properties.

707 Figure 10 shows a violin plot of in situ measured precipitation properties at different altitudes and
708 retrieved precipitation properties below the lidar-inferred cloud base. For each dataset, the white
709 dot represents the median value, while the black bar represents the interquartile range. Perhaps
710 surprisingly rain rate decreases going downward from the top half of the cloud (i.e. the largest rain
711 rates are in the upper portion of the cloud). Medians of rain rate at the cloud top half, cloud bottom
712 half and below the cloud are of 0.021 mm hr⁻¹, 0.008 mm hr⁻¹, and 0.001 mm hr⁻¹. Similar to rain
713 rate, there is also a decrease in precipitation number concentration (N_{precip}) and precipitation liquid
714 water content (LWC_{precip}) moving downward from the top half of the cloud. In contrast, D_{precip} and
715 σ_{precip} increase moving downward, that is bigger particles in the bottom half, and (just) below cloud.
716 Overall, the retrieved precipitation properties (below the cloud base) compare well with the in situ
717 estimates from the sawtooth below-cloud segments.

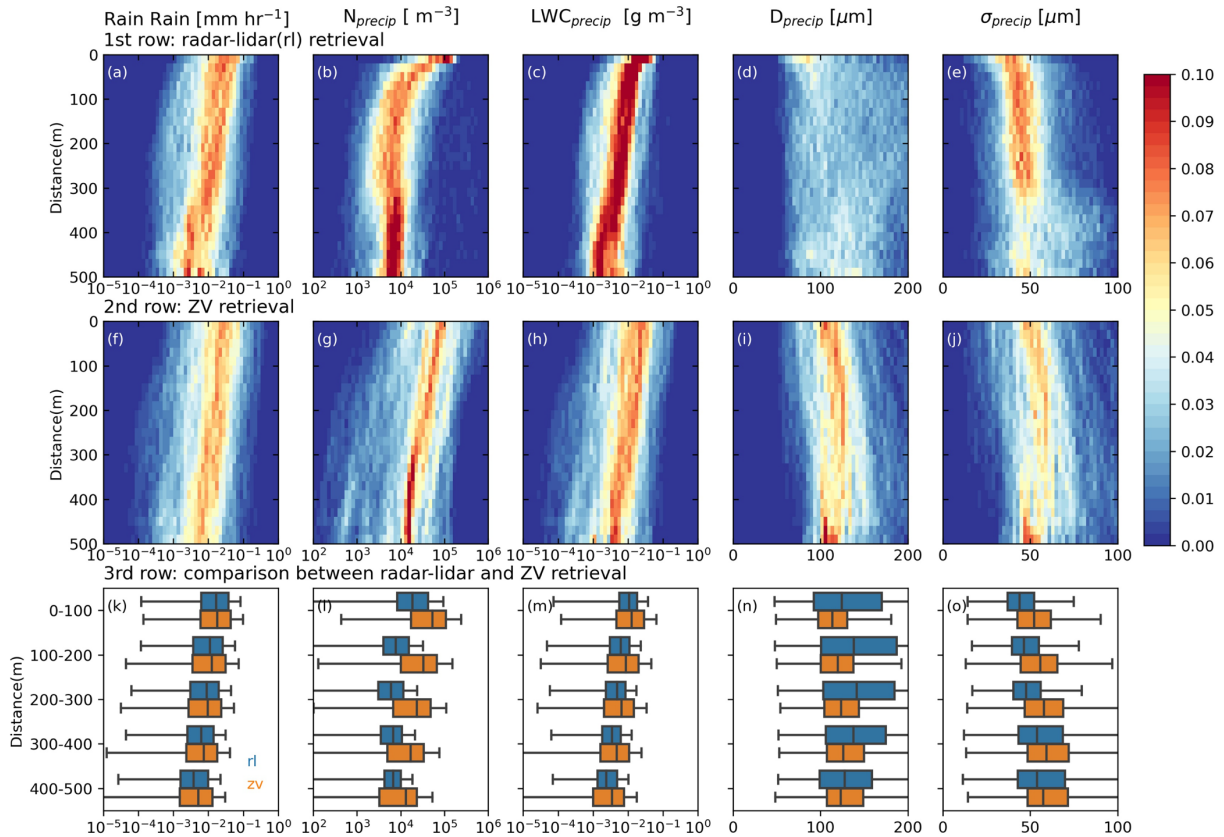
718 How do precipitation properties vary below cloud base? Figure 11 provides a more detailed view
719 on the vertical distribution of precipitation properties below cloud base. Here, the column shows
720 rain rate, N_{precip} , LWC_{precip} , D_{precip} , and σ_{precip} , respectively. The first two rows are histograms for
721 radar-lidar and ZV retrievals, respectively. The last row is a box plot that summarizes both
722 retrievals by binning the data vertically every 100 meters. Here, we only consider data in those
723 radar columns where rain extend at least 400m below cloud base. Overall, both the mean rain rate
724 and LWC_{precip} decrease exponentially with distance (as the change in the position of the distribution
725 peak is roughly linear with distance on a log-scale). Both retrievals have similar values and rates
726 of decrease (panel k and panel m). The e-folding distance over which the rain rate decrease to 1/e

727 (37%) of its initial value is about 260m for radar-lidar retrieval and 340 m for ZV retrieval. N_{precip}
 728 also decreases with distance, but we find the radar-lidar retrieval decreases more rapidly within
 729 the 200m below the cloud base, and the ZV retrieval shows higher N_{precip} than radar-lidar retrieval
 730 at different levels. This is consistent with (a result of) assuming a shape factor of zero in the ZV
 731 retrievals. The mean D_{precip} and σ_{precip} both increase with distance. Compared to radar-lidar
 732 retrieved D_{precip} , ZV retrieved D_{precip} is smaller overall (again consistent with the assumed shape
 733 factor), and has much less spread (variation) at any given altitude. Figure 10d shows that radar-
 734 lidar retrieved D_{precip} compare better with the in situ estimated D_{precip} from the below-cloud portion
 735 of the sawtooth legs than the ZV retrieved D_{precip} .



736
 737 **Figure 10.** Violin plot for in situ measured precipitation properties at different altitudes and
 738 retrieved precipitation properties below cloud base: (a) rain rate (or precipitation liquid water
 739 flux), (b) precipitation number concentration N_{precip} , (c) precipitation liquid water content
 740 LWC_{precip} , (d) precipitation liquid water content weighted mean diameter D_{precip} , (e) precipitation
 741 liquid water content weighted width σ_{precip} . A violin plot can be regarded as a hybrid of a boxplot

742 and a kernel density plot. For each dataset, the white dot represents the median value, while the
 743 black bar represents the interquartile range, and the outer shape is the kernel density estimation
 744 to show the distribution of the data. In situ measured precipitation properties are from these legs
 745 (as marked in Figure S1): the top half of the cloud layer from sawtooth legs (sawtooth top); the
 746 bottom half of the cloud layer from sawtooth legs (sawtooth bottom); the below-cloud portion of
 747 the sawtooth legs (sawtooth below-cloud); and in-cloud level legs.
 748
 749
 750



751
 752 **Figure 11.** Vertical distributions of below-cloud-base precipitation properties from retrievals
 753 (each column is rain rate, N_{precip} , LWC_{precip} , D_{precip} , σ_{precip} respectively). The first and second row
 754 is the histogram of retrieved precipitation properties below-cloud-base (data are normalized at each
 755 level), and y axis is the distance away from the cloud-base. First row is the results from radar-lidar
 756 retrievals, the second row is the results from ZV retrievals. The last row is the box plot that
 757 summarized the data in the first two rows by binned the data vertically every 100 meters, where
 758 blue boxes are from radar-lidar retrievals, and orange boxes are from ZV retrievals.
 759
 760

761 **6 Rain rate dependence on cloud depth and aerosol concentration**

762 In this section, we examine the degree to which precipitation can be diagnosed from cloud depth
 763 and cloud droplet or aerosol number concentration in the form (e.g. Comstock et al., 2004; Terai
 764 et al., 2012; Mann et al., 2014)

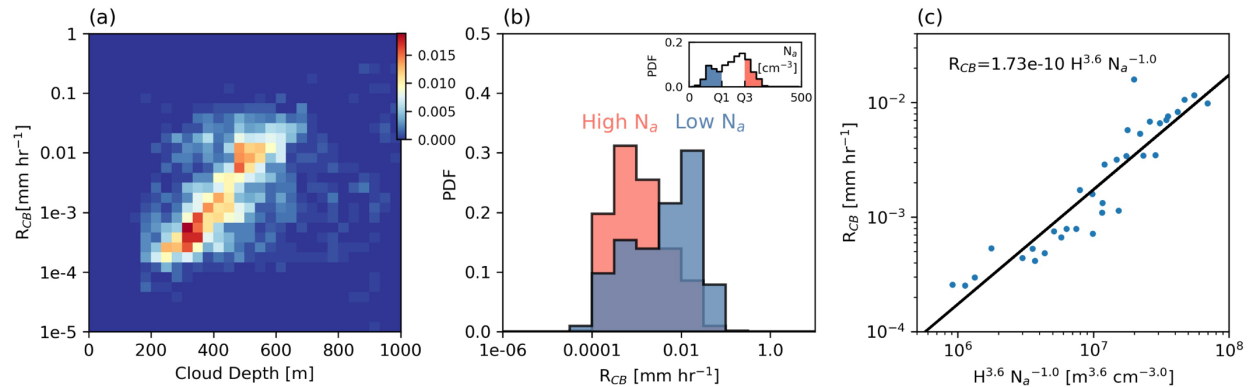
$$R_{CB} = k H^\alpha N^\beta \quad (11)$$

765 where N is usually the cloud droplet (N_d) or aerosol number concentrations (N_a), and H is cloud
 766 depth or liquid water path, and R_{CB} is rain rate at cloud base. To our knowledge, such a relationship
 767 has not been examined over the SO, except by Mace and Avey (2007) who used satellite retrievals.
 768 To examine this relationship over the SO, we use radar-lidar retrieved rain rate for R_{CB} , use the
 769 difference between cloud top and cloud base for H , and use accumulation mode aerosol
 770 concentrations with diameters larger than 70 nm from UHSAS for N_a .

771 First, we broadly examine the rain rate dependence on either cloud depth or aerosol concentration,
 772 individually. Figure 12a shows a joint histogram of rain rate at cloud base and cloud depth. The
 773 histogram shows that rain rate (at cloud base) scales with cloud depth, such that thicker clouds are
 774 associated with higher rain rates. This is consistent with previous studies (e.g. vanZanten et al.,
 775 2005; Pawlowska and Brenguier, 2003; Geoffroy et al., 2008). And to demonstrate the rain rate
 776 dependence on aerosol concentration, Figure 12b shows the probability density function of rain
 777 rate partitioned for conditions with low aerosol concentrations (lower than the first quartile,
 778 marked as blue) and high aerosol concentrations (higher than the third quartile, marked as red).
 779 Figure 12b shows that overall higher aerosol concentrations are associated with lower rain rates,
 780 consistent with aerosol suppression of precipitation.

781 How does rain rate relate to both cloud depth and aerosol concentration? To derive the coefficients
 782 in equation (11), we divided cloud depth (H) up to 600m into 6 bins, and divided aerosol
 783 concentrations (N_a) into 4 bins, and calculated the median rain rate for each H and N_a pair. Then
 784 we performed linear least square regression on the natural logarithms of data from these 24 bins
 785 (Figure 12c). The derived relationship is $R_{CB} = 1.73 \times 10^{-10} H^{3.6} N_a^{-1}$, with H in m, N_a in cm^{-3} ,
 786 and R_{CB} in mm hr^{-1} . Using bootstrap resampling technique, we estimate that the exponent α (one
 787 sigma uncertainty) for H range from 3.4 to 3.9, while the exponent β for N_a range from -1.3 to -
 788 0.8. The relationship we derive here is broadly similar to previous studies for stratocumulus in
 789 other regions. Exponent α for cloud depth typically is about 3 (vanZanten et al., 2005; Pawlowska
 790 and Brenguier, 2003; Lu et al., 2009), and the exponent β for number concentration (cloud droplet
 791 concentration or cloud condensation nuclei) typically ranges between -1.75 to -0.66 (vanZanten et
 792 al 2005; Mann et al., 2014; Lu et al., 2009; Comstock et al., 2004). The exponent β of -1 for aerosol
 793 concentration we derived here is smaller than exponent β of -0.32 in Mace and Avey (2017,
 794 hereafter M17), estimated using satellite-estimated cloud droplet number concentration, liquid
 795 water path, and rain rate for the SO. We will discuss this difference further at the of the next
 796 section.

797



798
 799 **Figure 12.** (a) Histogram of rain rate plotted as a function of cloud depth. (b) The probability
 800 density function of rain rate for conditions with low aerosol concentrations (lower than the first
 801 quartile, marked as blue) and high aerosol concentrations (higher than the third quartile, marked
 802 as red). (c) The rain rate at the cloud base is plotted as a function of the cloud depth, H , and aerosol
 803 concentration, N_a . Here H and N_a are the middle points for each cloud depth and aerosol
 804 concentration bin, while the rain rate at the cloud base is taken as the median value of rain rates in
 805 each cloud depth and aerosol concentration bin. The solid line shows the parametrization described
 806 in the main text.

807
 808

809 7 Conclusions

810 In this study, we examine in-and-below-cloud precipitation properties for stratocumulus over the
 811 Southern Ocean (SO), leveraging data collected from airborne W-band Cloud Radar (HCR), High
 812 Spectral Resolution Lidar (HSRL), and various in situ probes during the Southern Ocean Clouds
 813 Radiation Aerosol Transport Experimental Study (SOCRATES) in January-February 2018.

814 Overall, we find that about 60% of the stratocumulus were precipitating, and about 80% of the
 815 stratocumulus to be cold-topped (with a cloud top temperature $< 0^\circ\text{C}$) based on periods where the
 816 aircraft were flying below cloud and the radar and lidar pointing toward zenith. We determine the
 817 precipitation phase using the lidar particle linear depolarization ratio PLDR and find that about 60%
 818 of the precipitation is liquid phase, and about 20% of the precipitation is ice phase, with the
 819 remaining 20% being ambiguous. While we can not rule out the possibility that any individual
 820 ambiguous cases is pure liquid, most of such cases are likely to have ice or mixed phase
 821 precipitation present. Further, for cold-topped cloud, we find that when the reflectivity factor is
 822 less than about -10 dBZ, the precipitation is predominately liquid, while reflectivity factors greater
 823 than 0 dBZ, precipitation is predominately ice. This results is similar to what was found by Mace
 824 and Protat (2018) based on CAPRICORN data the during March-April 2016, as well as a recent
 825 study by Tansey et al. (2023) based on surface data collected at Macquarie Island (54.5°S) between
 826 March and November 2016. The SOCRATES data, collected in the Southern Hemisphere Summer,
 827 in January and February 2018, suggest this relationship is likely characteristic of SO low clouds
 828 through the year, and suggests that the measured reflectivity factor might be used as a proxy to
 829 determine the precipitation phase for *cold-topped Southern Ocean stratocumulus* with CloudSat
 830 (or other “radar only”) retrievals where no other information is available to constrain the
 831 precipitation phase.

832 For liquid-phase precipitation, we performed retrievals for precipitation rain rate and other
833 microphysical parameters based on cloud radar and lidar, with the goal to testing a hierarchy of
834 retrieval methods, from the simplest Z-R relationship approach where only radar reflectivity (Z) is
835 used to estimate the rain rate, to a reflectivity-velocity (ZV) retrieval where there are two
836 observables (inputs to the retrieval), to a radar-lidar retrieval with three observables. Our
837 evaluation show that rain rate from the Z-R, ZV , and radar-lidar retrievals all compare well with
838 the in situ, with Pearson correlation coefficient of 0.83, 0.88 and 0.68, and fractional difference
839 (difference between the retrieved and in situ median value divided by the average of the medians)
840 of only -8.0%, -4.6%, and 6.3%, respectively. In addition to rain rate, ZV and radar-lidar retrievals
841 can retrieve other precipitation properties, such as, precipitation number concentration,
842 precipitation liquid water content, number concentration, size and width. The overall statistics and
843 distribution of these retrieved precipitation properties below the cloud base, also compare well
844 with in situ estimates from the sawtooth below-cloud segments. This good performance gives us
845 some confidence in using these retrieval techniques for SO stratocumulus, including in our recently
846 published manuscript that examines coalescence scavenging in SO stratocumulus [Kang et al.,
847 2022].

848 Despite the good retrieval performance overall, there are important caveats. When developing the
849 power-law relationships between reflectivity (Z) and rain rate (R) following $Z = aR^b$ we found
850 the b exponent varied little with altitude and had a value around 1.3 to 1.4. This is similar to values
851 obtained in previous studies for stratocumulus in other regions (Comstock et al., 2004; vanZanten
852 et al., 2005). The a coefficient, on the other hand, increases as one moves from the cloud layer to
853 the surface. In general, one can derived a power-law relationship between Z and R based on the
854 assumption of a modified gamma distribution (e.g., Rosenfeld and Ulbrich 2003) and doing so
855 shows that one should expected the a coefficient to depend on the total droplet number
856 concentration. Given the vertical variations in the precipitation droplet number concentration (see
857 Figures 10 and 11), the vertical variation in the a coefficient is not surprising. But such also hints
858 that the a coefficient may well vary with the accumulation mode aerosol concentration or other
859 factors than control the cloud droplet number concentration. So Z-R relationships should be used
860 with some caution in studies intending to establish relationships between rain rates and aerosols.
861 We also find that the derived the derived Z-R relationships are sensitive to whether ones exclude
862 drops with diameters around 10-40 μm when in cloud, because these drops make a non-trivial
863 contribution to drizzle flux, as perhaps first noted by Nicholls (1984). Our analysis suggests that
864 below-cloud Z-R equations should be applied with caution to in-cloud reflectivity measurements,
865 and should be expected to underestimate the total liquid water flux in cloud.

866 Comparing the ZV retrieval with radar-lidar retrieval shows that both retrievals capture the mean
867 vertical structure of precipitation microphysics below cloud. Based on in situ data and retrievals,
868 we found that rain rate, precipitation number concentration (N_{precip}), precipitation liquid water
869 (LWC_{precip}) all decreases as one get closer to the surface, while precipitation liquid water content
870 weighted mean diameter (D_{precip}) and width (σ_{precip}) increases. The e-folding distance over which
871 the rain rate decrease to $1/e$ (37%) of its initial value is about 260m for radar-lidar retrieval and
872 340 m for ZV retrieval. However, we find that both D_0 and N_{precip} from the ZV retrieval have less
873 spatial variability than that from the radar-lidar retrieval, and assuming a shape factor of $\mu = 0$,
874 results in the ZV retrieved mean D_0 being a bit too small and N_{precip} being too large as compared
875 to the radar-lidar retrieval. This is because the shape factor is not constant and in particular,
876 because the shape factor in the stronger precipitation shafts below the thicker portion of the clouds

877 should be larger than zero (because the precipitation DSD is narrower with a more well defined
878 peaked rather than a broad exponential-like distribution).

879 This study also explored rain rate dependence on cloud depth and aerosol concentration. Rain rate
880 at cloud base (R_{CB}) increases with cloud depth (H) and decreases with aerosol concentration (N_a).
881 Using a least-squares regression, we found R_{CB} varies as $H^{3.6} N_a^{-1}$, which is broadly consistent
882 with estimates for stratocumulus in previous studies over other regions (vanZanten et al., 2005;
883 Pawlowska & Brenguier, 2003; Lu et al., 2009; Mann et al., 2014; Lu et al., 2009; Comstock et al.,
884 2004). However as noted in section 6, our results differ with the satellite-based estimates for the
885 SO by Mace and Avey (2007), hereafter M17, who suggest an exponent of -0.32 for the aerosol
886 concentration based on satellite retrievals. M17 also noted that their estimates differ from previous
887 studies in other regions. There are a variety of potential reasons for the different results in our
888 study and in M17. The first obvious reason is different data sources. Our study used in situ
889 measured N_a and retrieved rain rate with airborne radar and lidar measurements, while M17 used
890 N_a , liquid water path and rain rate derived from MODIS and Cloudsat based on an optimal
891 estimation algorithm. Another reason might be different cloud populations; where in our study
892 about 80% of the clouds are cold-topped, M17 restricted their analysis to warm-topped clouds.
893 Data collected during the Macquarie Island Cloud and Radiation Experiment (MICRE), suggest
894 that warm topped SO clouds are geometrically thinner and closer to the surface than cold-topped
895 clouds [Tansey et al., 2023, submitted]. As-is, we end this study here, leaving a regime-dependent
896 analysis of precipitation susceptibility for a future study. As more data is collected, including in
897 future campaigns such as the upcoming Clouds And Precipitation Experiment at Kennaook
898 (CAPE-K) that will begin in March 2024, the aerosol sensitivity of low altitude SO clouds is
899 certain to be focus of future multi- or cross-experiments studies.

900 **Acknowledgments**

901 This work was supported by the U.S. National Science Foundation on grant AGS-2124993. We
902 would like to thank the contribution from the many individuals and teams associated with the
903 NCAR Earth Observing Laboratory, SOCRATES Science and Aircraft Instrument Teams. We
904 thank Dr. Ulrike Romatschke for helping with radar data processing. We also would like to thank
905 open-source codes such as miopython and CloudnetPy.

907 **Open Research**

908 The authors would like to acknowledge the SOCRATES Project for providing data through the
909 SOCRATES Data Archive Center (SDAC) at NCAR's Earth Observing Laboratory: (1) low rate
910 (1 Hz) navigation, state parameter, and microphysics flight-level data (contain data from many
911 probes, including CDP and UHSAS) version 1.4 <https://data.eol.ucar.edu/dataset/552.002>; (2) 2DS
912 data version 1.1 (1 Hz) <https://data.eol.ucar.edu/dataset/552.047>; (3) HCR radar and HSRL lidar
913 moments data (2 Hz) <https://data.eol.ucar.edu/dataset/552.034>. Miopython is available at
914 <https://miopython.readthedocs.io/en/latest/>.

916

917

918 **References**

- 919 Arabzadeh, A., Ehsani, M. R., Guan, B., Heflin, S., & Behrangi, A. (2020). Global
 920 Intercomparison of Atmospheric Rivers Precipitation in Remote Sensing and Reanalysis
 921 Products. *Journal of Geophysical Research: Atmospheres*, *125*(21), e2020JD033021.
 922 <https://doi.org/10.1029/2020JD033021>
- 923 Bai, H., Gong, C., Wang, M., Zhang, Z., & L'Ecuyer, T. (2018). Estimating precipitation
 924 susceptibility in warm marine clouds using multi-sensor aerosol and cloud products from
 925 A-Train satellites. *Atmospheric Chemistry and Physics*, *18*(3), 1763–1783.
 926 <https://doi.org/10.5194/acp-18-1763-2018>
- 927 Beard, K. V. (1976). Terminal Velocity and Shape of Cloud and Precipitation Drops Aloft.
 928 *Journal of the Atmospheric Sciences*, *33*(5), 851–864. [https://doi.org/10.1175/1520-0469\(1976\)033<0851:TVASOC>2.0.CO;2](https://doi.org/10.1175/1520-0469(1976)033<0851:TVASOC>2.0.CO;2)
- 930 Behrangi, A., Lebsock, M., Wong, S., & Lambriksen, B. (2012). On the quantification of
 931 oceanic rainfall using spaceborne sensors. *Journal of Geophysical Research:*
 932 *Atmospheres*, *117*(D20). <https://doi.org/10.1029/2012JD017979>
- 933 Behrangi, A., Stephens, G., Adler, R. F., Huffman, G. J., Lambriksen, B., & Lebsock, M.
 934 (2014). An Update on the Oceanic Precipitation Rate and Its Zonal Distribution in Light
 935 of Advanced Observations from Space. *Journal of Climate*, *27*(11), 3957–3965.
 936 <https://doi.org/10.1175/JCLI-D-13-00679.1>
- 937 Bellouin, N., Quaas, J., Gryspeerdt, E., Kinne, S., Stier, P., Watson-Parris, D., et al. (2020).
 938 Bounding Global Aerosol Radiative Forcing of Climate Change. *Reviews of Geophysics*,
 939 *58*(1), e2019RG000660. <https://doi.org/10.1029/2019RG000660>
- 940 Bjordal, J., Storelvmo, T., Alterskjær, K., & Carlsen, T. (2020). Equilibrium climate sensitivity
 941 above 5 °C plausible due to state-dependent cloud feedback. *Nature Geoscience*, *13*(11),
 942 718–721. <https://doi.org/10.1038/s41561-020-00649-1>
- 943 Bodas-Salcedo, A., Hill, P. G., Furtado, K., Williams, K. D., Field, P. R., Manners, J. C., et al.
 944 (2016). Large Contribution of Supercooled Liquid Clouds to the Solar Radiation Budget
 945 of the Southern Ocean. *Journal of Climate*, *29*(11), 4213–4228.
 946 <https://doi.org/10.1175/JCLI-D-15-0564.1>
- 947 Bohren, C. F., & Huffman, D. R. (1983). Absorption and scattering of light by small particles.
 948 Weinheim: Wiley : Wiley Online Library.
- 949 Bromwich, D. H., Nicolas, J. P., & Monaghan, A. J. (2011). An Assessment of Precipitation
 950 Changes over Antarctica and the Southern Ocean since 1989 in Contemporary Global
 951 Reanalyses. *Journal of Climate*, *24*(16), 4189–4209.
 952 <https://doi.org/10.1175/2011JCLI4074.1>
- 953 Cesana, G. V., Khadir, T., Chepfer, H., & Chiriaco, M. (2022). Southern Ocean Solar Reflection
 954 Biases in CMIP6 Models Linked to Cloud Phase and Vertical Structure Representations.
 955 *Geophysical Research Letters*, *49*(22), e2022GL099777.
 956 <https://doi.org/10.1029/2022GL099777>
- 957 Comstock, K. K., Wood, R., Yuter, S. E., & Bretherton, C. S. (2004). Reflectivity and rain rate in
 958 and below drizzling stratocumulus. *Quarterly Journal of the Royal Meteorological*
 959 *Society*, *130*(603), 2891–2918. <https://doi.org/10.1256/qj.03.187>
- 960 de Lavergne, C., Palter, J. B., Galbraith, E. D., Bernardello, R., & Marinov, I. (2014). Cessation
 961 of deep convection in the open Southern Ocean under anthropogenic climate change.
 962 *Nature Climate Change*, *4*(4), 278–282. <https://doi.org/10.1038/nclimate2132>

- 963 DMT. (2013). Ultra high sensitivity aerosol spectrometer (UHSAS) Operator Manual.
 964 Eastman, R., Lebsock, M., & Wood, R. (2019). Warm Rain Rates from AMSR-E 89-GHz
 965 Brightness Temperatures Trained Using CloudSat Rain-Rate Observations. *Journal of*
 966 *Atmospheric and Oceanic Technology*, 36(6), 1033–1051.
 967 <https://doi.org/10.1175/JTECH-D-18-0185.1>
- 968 Ellis, S. M., Tsai, P., Burghart, C., Romatschke, U., Dixon, M., Vivekanandan, J., et al. (2019).
 969 Use of the Earth’s Surface as a Reference to Correct Airborne Nadir-Looking Radar
 970 Radial Velocity Measurements for Platform Motion. *Journal of Atmospheric and Oceanic*
 971 *Technology*, 36(7), 1343–1360. <https://doi.org/10.1175/JTECH-D-19-0019.1>
- 972 Ellis, T. D., L’Ecuyer, T., Haynes, J. M., & Stephens, G. L. (2009). How often does it rain over
 973 the global oceans? The perspective from CloudSat. *Geophysical Research Letters*, 36(3).
 974 <https://doi.org/10.1029/2008GL036728>
- 975 Eloranta, E. E. (2005). High Spectral Resolution Lidar. In C. Weitkamp (Ed.), *Lidar: Range-*
 976 *Resolved Optical Remote Sensing of the Atmosphere* (pp. 143–163). New York, NY:
 977 Springer. https://doi.org/10.1007/0-387-25101-4_5
- 978 Feingold, G., McComiskey, A., Rosenfeld, D., & Sorooshian, A. (2013). On the relationship
 979 between cloud contact time and precipitation susceptibility to aerosol. *Journal of*
 980 *Geophysical Research: Atmospheres*, 118(18), 10,544–10,554.
 981 <https://doi.org/10.1002/jgrd.50819>
- 982 Frisch, A. S., Fairall, C. W., & Snider, J. B. (1995). Measurement of Stratus Cloud and Drizzle
 983 Parameters in ASTEX with a K α -Band Doppler Radar and a Microwave Radiometer.
 984 *Journal of the Atmospheric Sciences*, 52(16), 2788–2799. [https://doi.org/10.1175/1520-0469\(1995\)052<2788:MOSCAD>2.0.CO;2](https://doi.org/10.1175/1520-0469(1995)052<2788:MOSCAD>2.0.CO;2)
- 985 Frölicher, T. L., Sarmiento, J. L., Paynter, D. J., Dunne, J. P., Krasting, J. P., & Winton, M.
 986 (2015). Dominance of the Southern Ocean in Anthropogenic Carbon and Heat Uptake in
 987 CMIP5 Models. *Journal of Climate*, 28(2), 862–886. <https://doi.org/10.1175/JCLI-D-14-00117.1>
- 988 Fyfe, J. C., Gillett, N. P., & Marshall, G. J. (2012). Human influence on extratropical Southern
 989 Hemisphere summer precipitation. *Geophysical Research Letters*, 39(23).
 990 <https://doi.org/10.1029/2012GL054199>
- 991 Ghate, V. P., & Cadetdu, M. P. (2019). Drizzle and turbulence below closed cellular marine
 992 stratocumulus clouds. *Journal of Geophysical Research-Atmospheres*, 124(11),
 993 2018JD030141. <https://doi.org/10.1029/2018JD030141>
- 994 Grecu, M., Olson, W. S., Munchak, S. J., Ringerud, S., Liao, L., Haddad, Z., et al. (2016). The
 995 GPM Combined Algorithm. *Journal of Atmospheric and Oceanic Technology*, 33(10),
 996 2225–2245. <https://doi.org/10.1175/JTECH-D-16-0019.1>
- 997 Hamilton, D. S., Lee, L. A., Pringle, K. J., Reddington, C. L., Spracklen, D. V., & Carslaw, K. S.
 998 (2014). Occurrence of pristine aerosol environments on a polluted planet. *Proceedings of*
 999 *the National Academy of Sciences*, 111(52), 18466–18471.
 1000 <https://doi.org/10.1073/pnas.1415440111>
- 1001 Hayden, L., & Liu, C. (2018). A Multiyear Analysis of Global Precipitation Combining
 1002 CloudSat and GPM Precipitation Retrievals. *Journal of Hydrometeorology*, 19(12),
 1003 1935–1952. <https://doi.org/10.1175/JHM-D-18-0053.1>
- 1004 Haynes, J. M., L’Ecuyer, T. S., Stephens, G. L., Miller, S. D., Mitrescu, C., Wood, N. B., &
 1005 Tanelli, S. (2009). Rainfall retrieval over the ocean with spaceborne W-band radar.
 1006
 1007

- 1008 *Journal of Geophysical Research: Atmospheres*, 114(D8).
1009 <https://doi.org/10.1029/2008JD009973>
- 1010 Kang, L., Marchand, R. T., Wood, R., & McCoy, I. L. (2022). Coalescence Scavenging Drives
1011 Droplet Number Concentration in Southern Ocean Low Clouds. *Geophysical Research*
1012 *Letters*, 49(7), e2022GL097819. <https://doi.org/10.1029/2022GL097819>
- 1013 Kang, L., Marchand, R., & Smith, W. (2021). Evaluation of MODIS and Himawari-8 Low
1014 Clouds Retrievals Over the Southern Ocean With In Situ Measurements From the
1015 SOCRATES Campaign. *Earth and Space Science*, 8(3), e2020EA001397.
1016 <https://doi.org/10.1029/2020EA001397>
- 1017 Khatiwala, S., Primeau, F., & Hall, T. (2009). Reconstruction of the history of anthropogenic
1018 CO₂ concentrations in the ocean. *Nature*, 462(7271), 346–349.
1019 <https://doi.org/10.1038/nature08526>
- 1020 Klepp, C., Michel, S., Protat, A., Burdanowitz, J., Albern, N., Kähnert, M., et al. (2018).
1021 OceanRAIN, a new in-situ shipboard global ocean surface-reference dataset of all water
1022 cycle components. *Scientific Data*, 5(1), 180122. <https://doi.org/10.1038/sdata.2018.122>
- 1023 Lance, S., Brock, C. A., Rogers, D., & Gordon, J. A. (2010). Water droplet calibration of the
1024 Cloud Droplet Probe (CDP) and in-flight performance in liquid, ice and mixed-phase
1025 clouds during ARCPAC. *Atmospheric Measurement Techniques*, 3(6), 1683–1706.
1026 <https://doi.org/10.5194/amt-3-1683-2010>
- 1027 Lang, F., Huang, Y., Siems, S. T., & Manton, M. J. (2018). Characteristics of the Marine
1028 Atmospheric Boundary Layer Over the Southern Ocean in Response to the Synoptic
1029 Forcing. *Journal of Geophysical Research: Atmospheres*, 123(15), 7799–7820.
1030 <https://doi.org/10.1029/2018JD028700>
- 1031 Lee, L. A., Reddington, C. L., & Carslaw, K. S. (2016). On the relationship between aerosol
1032 model uncertainty and radiative forcing uncertainty. *Proceedings of the National*
1033 *Academy of Sciences*, 113(21), 5820–5827. <https://doi.org/10.1073/pnas.1507050113>
- 1034 Lu, M.-L., Sorooshian, A., Jonsson, H. H., Feingold, G., Flagan, R. C., & Seinfeld, J. H. (2009).
1035 Marine stratocumulus aerosol-cloud relationships in the MASE-II experiment:
1036 Precipitation susceptibility in eastern Pacific marine stratocumulus. *Journal of*
1037 *Geophysical Research: Atmospheres*, 114(D24). <https://doi.org/10.1029/2009JD012774>
- 1038 Mace, G. G., & Avey, S. (2017). Seasonal variability of warm boundary layer cloud and
1039 precipitation properties in the Southern Ocean as diagnosed from A-Train data. *Journal of*
1040 *Geophysical Research: Atmospheres*, 122(2), 1015–1032.
1041 <https://doi.org/10.1002/2016JD025348>
- 1042 Mace, G. G., & Protat, A. (2018). Clouds over the Southern Ocean as Observed from the R/V
1043 Investigator during CAPRICORN. Part I: Cloud Occurrence and Phase Partitioning.
1044 *Journal of Applied Meteorology and Climatology*, 57(8), 1783–1803.
1045 <https://doi.org/10.1175/JAMC-D-17-0194.1>
- 1046 Mace, G. G., Heymsfield, A. J., & Poellot, M. R. (2002). On retrieving the microphysical
1047 properties of cirrus clouds using the moments of the millimeter-wavelength Doppler
1048 spectrum. *Journal of Geophysical Research: Atmospheres*, 107(D24), AAC 22-1-AAC
1049 22-26. <https://doi.org/10.1029/2001JD001308>
- 1050 Mann, J. A. L., Christine Chiu, J., Hogan, R. J., O'Connor, E. J., L'Ecuyer, T. S., Stein, T. H.
1051 M., & Jefferson, A. (2014). Aerosol impacts on drizzle properties in warm clouds from
1052 ARM Mobile Facility maritime and continental deployments. *Journal of Geophysical*
1053 *Research: Atmospheres*, 119(7), 4136–4148. <https://doi.org/10.1002/2013JD021339>

- 1054 Manton, M. J., Huang, Y., & Siems, S. T. (2020). Variations in Precipitation across the Southern
 1055 Ocean. *Journal of Climate*, 33(24), 10653–10670. [https://doi.org/10.1175/JCLI-D-20-](https://doi.org/10.1175/JCLI-D-20-0120.1)
 1056 [0120.1](https://doi.org/10.1175/JCLI-D-20-0120.1)
- 1057 Marchand, R. T., Ackerman, T. P., & Moroney, C. (2007). An assessment of Multiangle Imaging
 1058 Spectroradiometer (MISR) stereo-derived cloud top heights and cloud top winds using
 1059 ground-based radar, lidar, and microwave radiometers. *Journal of Geophysical Research:*
 1060 *Atmospheres*, 112(D6). <https://doi.org/10.1029/2006JD007091>
- 1061 Marchand, R., Mace, G. G., Ackerman, T., & Stephens, G. (2008). Hydrometeor Detection
 1062 Using Cloudsat—An Earth-Orbiting 94-GHz Cloud Radar. *Journal of Atmospheric and*
 1063 *Oceanic Technology*, 25(4), 519–533. <https://doi.org/10.1175/2007JTECHA1006.1>
- 1064 McCoy, I. L., McCoy, D. T., Wood, R., Regayre, L., Watson-Parris, D., Grosvenor, D. P., et al.
 1065 (2020). The hemispheric contrast in cloud microphysical properties constrains aerosol
 1066 forcing. *Proceedings of the National Academy of Sciences of the United States of*
 1067 *America*, 117(32), 18998–19006. <https://doi.org/10.1073/pnas.1922502117>
- 1068 McFarquhar, G. M., Bretherton, C. S., Marchand, R., Protat, A., DeMott, P. J., Alexander, S. P.,
 1069 et al. (2021). Observations of Clouds, Aerosols, Precipitation, and Surface Radiation over
 1070 the Southern Ocean: An Overview of CAPRICORN, MARCUS, MICRE, and
 1071 SOCRATES. *Bulletin of the American Meteorological Society*, 102(4), E894–E928.
 1072 <https://doi.org/10.1175/BAMS-D-20-0132.1>
- 1073 Mitrescu, C., L’Ecuyer, T., Haynes, J., Miller, S., & Turk, J. (2010). CloudSat Precipitation
 1074 Profiling Algorithm—Model Description. *Journal of Applied Meteorology and*
 1075 *Climatology*, 49(5), 991–1003. <https://doi.org/10.1175/2009JAMC2181.1>
- 1076 Mohrmann, J., Wood, R., McGibbon, J., Eastman, R., & Luke, E. (2018). Drivers of Seasonal
 1077 Variability in Marine Boundary Layer Aerosol Number Concentration Investigated Using
 1078 a Steady State Approach. *Journal of Geophysical Research: Atmospheres*, 123(2), 1097–
 1079 1112. <https://doi.org/10.1002/2017JD027443>
- 1080 Montoya Duque, E., Huang, Y., Siems, S. T., May, P. T., Protat, A., & McFarquhar, G. M.
 1081 (2022). A Characterization of Clouds and Precipitation Over the Southern Ocean From
 1082 Synoptic to Micro Scales During the CAPRICORN Field Campaigns. *Journal of*
 1083 *Geophysical Research: Atmospheres*, 127(17), e2022JD036796.
 1084 <https://doi.org/10.1029/2022JD036796>
- 1085 Mülmenstädt, J., Salzmänn, M., Kay, J. E., Zelinka, M. D., Ma, P.-L., Nam, C., et al. (2021). An
 1086 underestimated negative cloud feedback from cloud lifetime changes. *Nature Climate*
 1087 *Change*, 11(6), 508–513. <https://doi.org/10.1038/s41558-021-01038-1>
- 1088 NCAR/EOL HCR Team. 2022. SOCRATES: NCAR HCR radar moments data. Version 3.1.
 1089 UCAR/NCAR - Earth Observing Laboratory. <https://doi.org/10.5065/D68914PH>.
- 1090 Nicholls, S. (1984). The dynamics of stratocumulus: Aircraft observations and comparisons with
 1091 a mixed layer model. *Quarterly Journal of the Royal Meteorological Society*, 110(466),
 1092 783–820. <https://doi.org/10.1002/qj.49711046603>
- 1093 Nicolas, J. P., & Bromwich, D. H. (2011). Precipitation Changes in High Southern Latitudes
 1094 from Global Reanalyses: A Cautionary Tale. *Surveys in Geophysics*, 32(4), 475–494.
 1095 <https://doi.org/10.1007/s10712-011-9114-6>
- 1096 O’Connor, E. J., Hogan, R. J., & Illingworth, A. J. (2005). Retrieving Stratocumulus Drizzle
 1097 Parameters Using Doppler Radar and Lidar. *Journal of Applied Meteorology and*
 1098 *Climatology*, 44(1), 14–27. <https://doi.org/10.1175/JAM-2181.1>

- 1099 Orr, B. W., & Kropfli, R. A. (1999). A Method for Estimating Particle Fall Velocities from
 1100 Vertically Pointing Doppler Radar. *Journal of Atmospheric and Oceanic Technology*,
 1101 16(1), 29–37. [https://doi.org/10.1175/1520-0426\(1999\)016<0029:AMFEPF>2.0.CO;2](https://doi.org/10.1175/1520-0426(1999)016<0029:AMFEPF>2.0.CO;2)
- 1102 Pauling, A. G., Bitz, C. M., Smith, I. J., & Langhorne, P. J. (2016). The Response of the
 1103 Southern Ocean and Antarctic Sea Ice to Freshwater from Ice Shelves in an Earth System
 1104 Model. *Journal of Climate*, 29(5), 1655–1672. <https://doi.org/10.1175/JCLI-D-15-0501.1>
- 1105 Pawlowska, H., & Brenguier, J.-L. (2003). An observational study of drizzle formation in
 1106 stratocumulus clouds for general circulation model (GCM) parameterizations. *Journal of*
 1107 *Geophysical Research: Atmospheres*, 108(D15). <https://doi.org/10.1029/2002JD002679>
- 1108 Protat, A., Klepp, C., Louf, V., Petersen, W. A., Alexander, S. P., Barros, A., et al. (2019a). The
 1109 Latitudinal Variability of Oceanic Rainfall Properties and Its Implication for Satellite
 1110 Retrievals: 1. Drop Size Distribution Properties. *Journal of Geophysical Research:*
 1111 *Atmospheres*, 124(23), 13291–13311. <https://doi.org/10.1029/2019JD031010>
- 1112 Protat, A., Klepp, C., Louf, V., Petersen, W. A., Alexander, S. P., Barros, A., et al. (2019b). The
 1113 Latitudinal Variability of Oceanic Rainfall Properties and Its Implication for Satellite
 1114 Retrievals: 1. Drop Size Distribution Properties. *Journal of Geophysical Research:*
 1115 *Atmospheres*, 124(23), 13291–13311. <https://doi.org/10.1029/2019JD031010>
- 1116 Romatschke, U., Dixon, M., Tsai, P., Loew, E., Vivekanandan, J., Emmett, J., & Rilling, R.
 1117 (2021). The NCAR Airborne 94-GHz Cloud Radar: Calibration and Data Processing.
 1118 *Data*, 6(6), 66. <https://doi.org/10.3390/data606066>
- 1119 Rosenfeld, D., & Ulbrich, C. W. (2003). Cloud Microphysical Properties, Processes, and Rainfall
 1120 Estimation Opportunities. *Meteorological Monographs*, 30(52), 237–258.
 1121 [https://doi.org/10.1175/0065-9401\(2003\)030<0237:CMPPAR>2.0.CO;2](https://doi.org/10.1175/0065-9401(2003)030<0237:CMPPAR>2.0.CO;2)
- 1122 Sanchez, K. J., Roberts, G. C., Saliba, G., Russell, L. M., Twohy, C., Reeves, J. M., et al. (2021).
 1123 Measurement report: Cloud processes and the transport of biological emissions affect
 1124 southern ocean particle and cloud condensation nuclei concentrations. *Atmospheric*
 1125 *Chemistry and Physics*, 21(5), 3427–3446. <https://doi.org/10.5194/acp-21-3427-2021>
- 1126 Sarkar, M., Zuidema, P., & Ghate, V. (2021). Clarifying Remotely Retrieved Precipitation of
 1127 Shallow Marine Clouds from the NSF/NCAR Gulfstream V. *Journal of Atmospheric and*
 1128 *Oceanic Technology*, 38(9), 1657–1670. <https://doi.org/10.1175/JTECH-D-20-0166.1>
- 1129 Sarmiento, J. L., Hughes, T. M. C., Stouffer, R. J., & Manabe, S. (1998). Simulated response of
 1130 the ocean carbon cycle to anthropogenic climate warming. *Nature*, 393(6682), 245–249.
 1131 <https://doi.org/10.1038/30455>
- 1132 Sassen, K., & Liao, L. (1996). Estimation of Cloud Content by W-Band Radar. *Journal of*
 1133 *Applied Meteorology and Climatology*, 35(6), 932–938. [https://doi.org/10.1175/1520-0450\(1996\)035<0932:EOCCBW>2.0.CO;2](https://doi.org/10.1175/1520-0450(1996)035<0932:EOCCBW>2.0.CO;2)
- 1134 Schwartz, M. C., Ghate, V. P., Albrecht, B. A., Zuidema, P., Cadetdu, M. P., Vivekanandan, J.,
 1135 et al. (2019). Merged Cloud and Precipitation Dataset from the HIAPER GV for the
 1136 Cloud System Evolution in the Trades (CSET) Campaign. *Journal of Atmospheric and*
 1137 *Oceanic Technology*, 36(6), 921–940. <https://doi.org/10.1175/JTECH-D-18-0111.1>
- 1138 Seto, S., Iguchi, T., & Oki, T. (2013). The Basic Performance of a Precipitation Retrieval
 1139 Algorithm for the Global Precipitation Measurement Mission’s Single/Dual-Frequency
 1140 Radar Measurements. *IEEE Transactions on Geoscience and Remote Sensing*, 51(12),
 1141 5239–5251. <https://doi.org/10.1109/TGRS.2012.2231686>

- 1143 Smalley, K. M., Lebsock, M. D., Eastman, R., Smalley, M., & Witte, M. K. (2022). A
 1144 Lagrangian analysis of pockets of open cells over the southeastern Pacific. *Atmospheric*
 1145 *Chemistry and Physics*, 22(12), 8197–8219. <https://doi.org/10.5194/acp-22-8197-2022>
- 1146 Stephens, G. L., L'Ecuyer, T., Forbes, R., Gettelmen, A., Golaz, J.-C., Bodas-Salcedo, A., et al.
 1147 (2010). Dreary state of precipitation in global models. *Journal of Geophysical Research:*
 1148 *Atmospheres*, 115(D24). <https://doi.org/10.1029/2010JD014532>
- 1149 Swart, N. C., Gille, S. T., Fyfe, J. C., & Gillett, N. P. (2018). Recent Southern Ocean warming
 1150 and freshening driven by greenhouse gas emissions and ozone depletion. *Nature*
 1151 *Geoscience*, 11(11), 836–841. <https://doi.org/10.1038/s41561-018-0226-1>
- 1152 Tan, I., Storelvmo, T., & Zelinka, M. D. (2016). Observational constraints on mixed-phase
 1153 clouds imply higher climate sensitivity. *Science*, 352(6282), 224–227.
 1154 <https://doi.org/10.1126/science.aad5300>
- 1155 Tansey, E., Marchand, R. T., Alexander, S. P., Klekociuk, A. R., & Protat, A. (2023). Southern
 1156 Ocean low cloud and precipitation phase observed during the Macquarie Island Cloud
 1157 and Radiation Experiment (MICRE) (preprint). Preprints.
 1158 <https://doi.org/10.22541/essoar.168394768.89694625/v1>
- 1159 Tansey, E., Marchand, R., Protat, A., Alexander, S. P., & Ding, S. (2022). Southern Ocean
 1160 Precipitation Characteristics Observed From CloudSat and Ground Instrumentation
 1161 During the Macquarie Island Cloud & Radiation Experiment (MICRE): April 2016 to
 1162 March 2017. *Journal of Geophysical Research: Atmospheres*, 127(5), e2021JD035370.
 1163 <https://doi.org/10.1029/2021JD035370>
- 1164 Terai, C. R., Wood, R., Leon, D. C., & Zuidema, P. (2012). Does precipitation susceptibility
 1165 vary with increasing cloud thickness in marine stratocumulus? *Atmospheric Chemistry*
 1166 *and Physics*, 12(10), 4567–4583. <https://doi.org/10.5194/acp-12-4567-2012>
- 1167 Trenberth, K. E., & Fasullo, J. T. (2010). Simulation of Present-Day and Twenty-First-Century
 1168 Energy Budgets of the Southern Oceans. *Journal of Climate*, 23(2), 440–454.
 1169 <https://doi.org/10.1175/2009JCLI3152.1>
- 1170 UCAR/NCAR - Earth Observing Laboratory. 2022. SOCRATES: Low Rate (LRT - 1 sps)
 1171 Navigation, State Parameter, and Microphysics Flight-Level Data. Version 1.4.
 1172 UCAR/NCAR - Earth Observing Laboratory. <https://doi.org/10.5065/D6M32TM9>.
- 1173 Vali, G., Kelly, R. D., French, J., Haimov, S., Leon, D., McIntosh, R. E., & Pazmany, A. (1998).
 1174 Finescale Structure and Microphysics of Coastal Stratus. *Journal of the Atmospheric*
 1175 *Sciences*, 55(24), 3540–3564. [https://doi.org/10.1175/1520-0469\(1998\)055<3540:FSAMOC>2.0.CO;2](https://doi.org/10.1175/1520-0469(1998)055<3540:FSAMOC>2.0.CO;2)
- 1176 vanZanten, M. C., Stevens, B., Vali, G., & Lenschow, D. H. (2005). Observations of Drizzle in
 1177 Nocturnal Marine Stratocumulus. *Journal of the Atmospheric Sciences*, 62(1), 88–106.
 1178 <https://doi.org/10.1175/JAS-3355.1>
- 1179 Vivekanandan, J., Ellis, S., Tsai, P., Loew, E., Lee, W.-C., Emmett, J., et al. (2015). A wing pod-
 1180 based millimeter wavelength airborne cloud radar. *Geoscientific Instrumentation,*
 1181 *Methods and Data Systems*, 4(2), 161–176. <https://doi.org/10.5194/gi-4-161-2015>
- 1182 von Terzi, L., Dias Neto, J., Ori, D., Myagkov, A., & Kneifel, S. (2022). Ice microphysical
 1183 processes in the dendritic growth layer: a statistical analysis combining multi-frequency
 1184 and polarimetric Doppler cloud radar observations. *Atmospheric Chemistry and Physics*,
 1185 22(17), 11795–11821. <https://doi.org/10.5194/acp-22-11795-2022>
- 1186 Wang, H., & Feingold, G. (2009). Modeling Mesoscale Cellular Structures and Drizzle in
 1187 Marine Stratocumulus. Part I: Impact of Drizzle on the Formation and Evolution of Open
 1188

- 1189 Cells. *Journal of the Atmospheric Sciences*, 66(11), 3237–3256.
1190 <https://doi.org/10.1175/2009JAS3022.1>
- 1191 Wilks, D. S. (1997). Resampling Hypothesis Tests for Autocorrelated Fields. *Journal of Climate*,
1192 10(1), 65–82. [https://doi.org/10.1175/1520-0442\(1997\)010<0065:RHTFAF>2.0.CO;2](https://doi.org/10.1175/1520-0442(1997)010<0065:RHTFAF>2.0.CO;2)
- 1193 Wiscombe, J. (1979). Mie Scattering Calculations: Advances in Technique and Fast, Vector-
1194 speed Computer Codes. <https://doi.org/10.5065/D6ZP4414>
- 1195 Wood, R. (2005). Drizzle in Stratiform Boundary Layer Clouds. Part II: Microphysical Aspects.
1196 *Journal of the Atmospheric Sciences*, 62(9), 3034–3050.
1197 <https://doi.org/10.1175/JAS3530.1>
- 1198 Wood, R., Bretherton, C. S., Leon, D., Clarke, A. D., Zuidema, P., Allen, G., & Coe, H. (2011).
1199 An aircraft case study of the spatial transition from closed to open mesoscale cellular
1200 convection over the Southeast Pacific. *Atmospheric Chemistry and Physics*, 11(5), 2341–
1201 2370. <https://doi.org/10.5194/acp-11-2341-2011>
- 1202 Wu, W., McFarquhar, G. 2019. NSF/NCAR GV HIAPER 2D-S Particle Size Distribution (PSD)
1203 Product Data. Version 1.1. UCAR/NCAR - Earth Observing Laboratory.
1204 <https://doi.org/10.26023/8HMG-WQP3-XA0X>.
- 1205 Yamaguchi, T., & Feingold, G. (2015). On the relationship between open cellular convective
1206 cloud patterns and the spatial distribution of precipitation. *Atmospheric Chemistry and*
1207 *Physics*, 15(3), 1237–1251. <https://doi.org/10.5194/acp-15-1237-2015>
- 1208 Yang, F., Luke, E. P., Kollias, P., Kostinski, A. B., & Vogelmann, A. M. (2018). Scaling of
1209 drizzle virga depth with cloud thickness for marine stratocumulus clouds. *Geophysical*
1210 *Research Letters*, 45(8), 3746–3753. <https://doi.org/10.1029/2018GL077145>
- 1211 Zelinka, M. D., Myers, T. A., McCoy, D. T., Po-Chedley, S., Caldwell, P. M., Ceppi, P., et al.
1212 (2020). Causes of Higher Climate Sensitivity in CMIP6 Models. *Geophysical Research*
1213 *Letters*, 47(1), e2019GL085782. <https://doi.org/10.1029/2019GL085782>
- 1214 Zhang, D., Wang, Z., Luo, T., Yin, Y., & Flynn, C. (2017). The occurrence of ice production in
1215 slightly supercooled Arctic stratiform clouds as observed by ground-based remote sensors
1216 at the ARM NSA site. *Journal of Geophysical Research: Atmospheres*, 122(5), 2867–
1217 2877. <https://doi.org/10.1002/2016JD026226>
- 1218 Zhou, X., Atlas, R., McCoy, I. L., Bretherton, C. S., Bardeen, C., Gettelman, A., et al. (2021).
1219 Evaluation of Cloud and Precipitation Simulations in CAM6 and AM4 Using
1220 Observations Over the Southern Ocean. *Earth and Space Science*, 8(2), e2020EA001241.
1221 <https://doi.org/10.1029/2020EA001241>
- 1222